ARTICLE

Integration of Multitargeted Polymer-Based Contrast Agents with Photoacoustic Computed Tomography: An Imaging Technique to Visualize Breast Cancer Intratumor Heterogeneity

Lei Li, Deepanjali Patil, Greg Petruncio, Kathleen K. Harnden, Jisha V. Somasekharan, Mikell Paige, Lihong V. Wang, and Carolina Salvador-Morales*

Cite This: https://dx.doi.org/10.1021/acsnano.0c05893

Read Online

ACCESS | Metrics & More | Article Recommendations | SI Supporting Information

ABSTRACT: One of the primary challenges in breast cancer diagnosis and treatment is intratumor heterogeneity (ITH), *i.e.*, the coexistence of different genetically and epigenetically distinct malignant cells within the same tumor. Thus, the identification of ITH is critical for designing better treatments and hence to increase patient survival rates. Herein, we report a noninvasive hybrid imaging technology that integrates multitargeted and multiplexed patchy polymeric photoacoustic contrast agents (MTMPPPCAs) with single-impulse panoramic photoacoustic computed tomography (SIP-PACT). The target specificity ability

of MTMPPPCAs to distinguish estrogen and progesterone receptor-positive breast tumors was demonstrated through both fluorescence and photoacoustic measurements and validated by tissue pathology analysis. This work provides the proof-of-concept of the MTMPPPCAs/SIP-PACT system to identify ITH in nonmetastatic tumors, with both high molecular specificity and real-time detection capability.

KEYWORDS: breast cancer, intratumor heterogeneity, multitargeted, single-impulse panoramic photoacoustic computed tomography, patchy particles
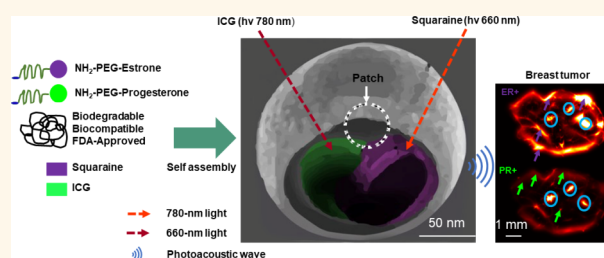
Breast cancer accounts for the second leading cause of cancer death globally (11.6%) with an alarming mortality rate of 6.6% as per 2018 global cancer statistics.[1,2] One of the primary challenges in breast cancer diagnosis and treatment is intratumor heterogeneity (ITH). ITH is the coexistence of different genetically and epigenetically distinct malignant cells within the same tumor.[3−5] It is responsible for 30% of cancer-related deaths worldwide in women, as it is closely associated with cancer progression, resistance to therapy, and recurrences.[6] The current treatment options for breast cancer are guided by critical factors, including molecular subtypes,[7,8] locations, metastatic stages, previous treatments, and other parameters.[3,4,6] Luminal A (LA), luminal B (LB), human epidermal growth factor receptor 2 (HER2)-enriched cells, and triple-negative breast cancer (TNBC) are the main subtypes treated in clinical settings.[9] LA and LB are present in 70% of breast cancer tumors,[10,11] whereas HER2 and TNBC are found in 15−30%

and 15% of breast cancers, respectively.[12−14] TNBC is the most aggressive subtype and has a worse prognosis than the other three.[15]

Currently, positron emission tomography/computed tomography (PET/CT) is the only imaging modality that is capable of rendering ITH information based on metabolic activity,[16−19] cell proliferation, and estrogen receptor (ER) status in breast cancer tumors.[20−22] However, the main challenges of using PET/CT include the high cost, long-term exposure to radiation, and the side effects of radiotracers. Furthermore,
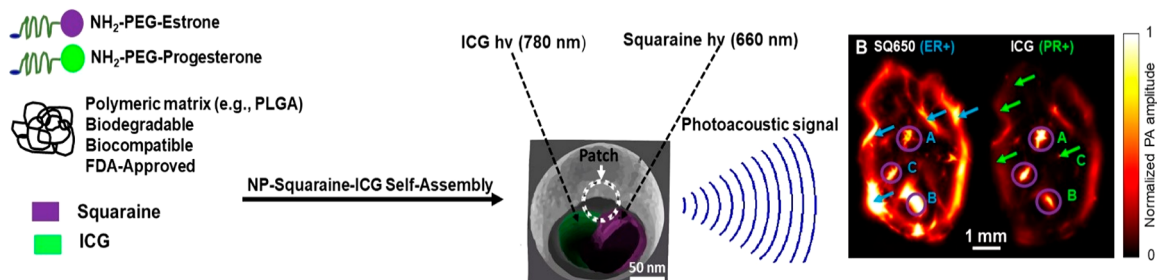
Figure 1. Design and functionality of MTMPPPCAs. The surface and patch of MTMPPPCAs were functionalized with NH_2-PEG-estrone and NH_2-PEG-progesterone. SQ650 and ICG formed the inner lining of MTMPPPCAs' core. The MTMPPPCAs exhibited two optical absorption peaks at 660 and 780 nm, respectively. Each absorption peak was linked to a specific targeting moiety. For example, the absorption peak at 660 nm indicates the specific binding of MTMPPPCAs functionalized with NH_2-PEG-estrone to the estrogen receptor.
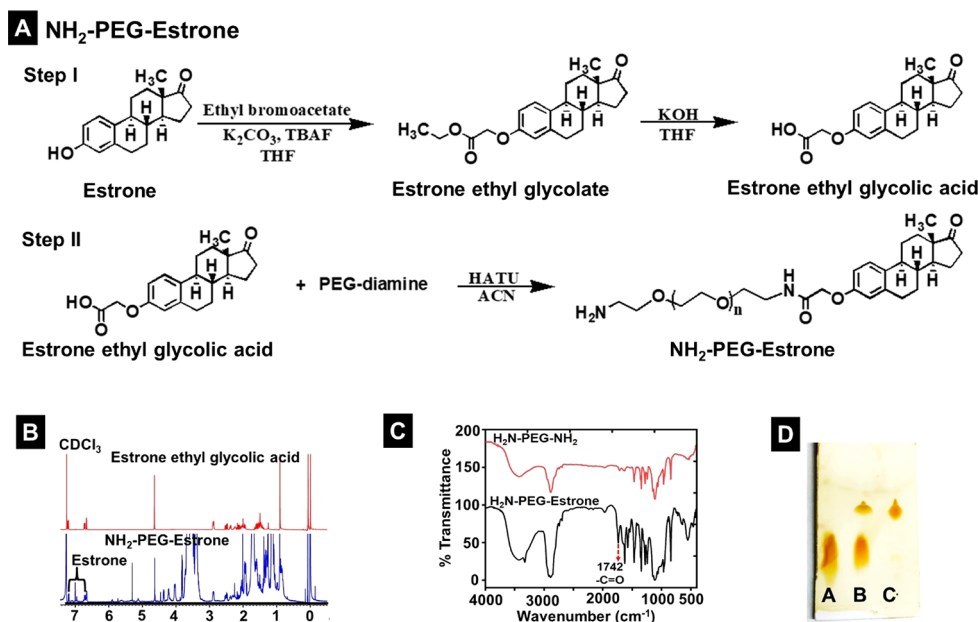
Figure 2. (A) Stepwise methodology for the synthesis of NH_2-PEG-estrone. Step I. Synthesis of estrone ethyl glycolic acid. Conditions: (1) Ethyl bromoacetate, K_2CO_3, TBAF, THF, HCl, 40 °C, overnight. (2) KOH, THF−H_2O (1:1), room temperature, overnight. Step II. Synthesis of NH_2-PEG-estrone. Conditions: HATU, anhydrous conditions, ACN, room temperature, overnight. Chemical characterization of PEGylated targeting moieties. (B) NH_2-PEG-estrone ^1H NMR. (C) FTIR. (D) TLC ((A) estrone ethyl glycolic acid, (B) co-spot, (C) NH_2-PEG-estrone).

although PET/CT can analyze different molecular subtypes of breast cancer, the exact localization of cancer cell receptors for identifying ITH requires additional confirmation from histology studies to avoid false-positive predictions.[23−26] Thus, there is an unmet critical need in oncology care for a noninvasive technology with multitargeting ability and high molecular specificity to localize and visualize ITH at non- and metastatic stages of breast cancer.

Photoacoustic tomography (PAT), paired with targeted contrast agents, holds a great potential to fill this clinical gap.[27−32] Until now, PAT, a noninvasive and ionizing-radiation-free technique, is the only high-resolution optical imaging modality that breaks the optical diffusion limit, which provides high spatiotemporal resolution and deep tissue penetration.[33−37] In PAT, the ultrasonic photoacoustic (PA) waves re-emitted by the tissue chromophores are subsequently detected to generate tomographic images with optical contrasts.[35,38−40] A recent advancement, single-impulse pan-oramic photoacoustic computed tomography (SIP-PACT), provides all the above-mentioned functionalities with high

molecular contrast.[41] Since abnormally increased vasculature and hemoglobin at tumor sites produce strong intrinsic PA contrast, PAT is ideally suited for visualizing angiogenesis and subsequently determining the intratumor heterogeneity.[42,43] Recently, it has been used to distinguish different molecular subtypes including LA, LB, and TNBC based on the overall tissue composition and physiological properties of breast cancer tumors.[44−46] Despite these enormous advances, PAT has not yet been established in clinical settings for the diagnosis and treatment of breast cancer.

Exploiting the molecular specificity offered by targeted nanoparticles can drive the development of high-throughput imaging probes for tumor visualization in real time.[47−49] Previously, we have developed patchy polymeric poly(lactic-co-glycolic acid) (PLGA) nanoparticles.[50] These are a class of anisotropic particles that have one or more surface-exposed domains with different surface chemistry relative to the rest of the particle.[50,51] A unique feature of multitargeted and multiplexed patchy polymeric photoacoustic contrast agents (MTMPPPCAs) is the patchy surface that makes the targeting
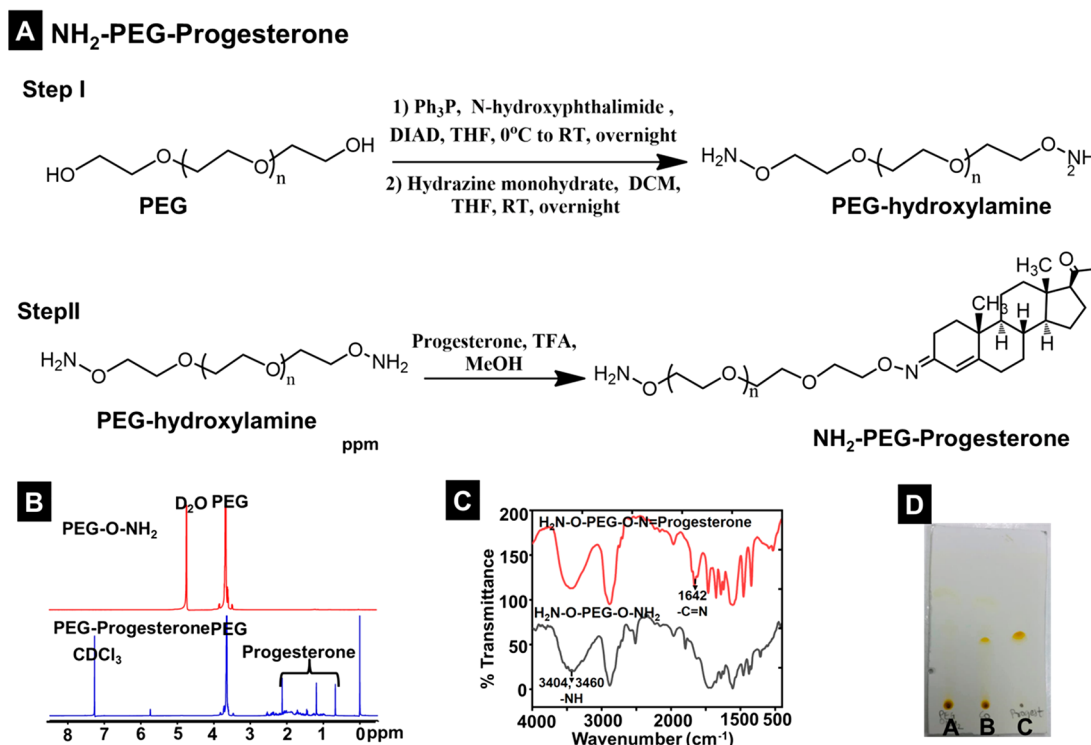
Figure 3. Synthesis and chemical characterization of NH₂-PEG-progesterone. (A) Synthesis of PEG-hydroxylamine. Step I. Conditions: (1) PPh₃, N-hydroxypthalimide, DIAD, THF, 0 °C to room temperature, overnight. (2) Hydrazine monohydrate, THF, reflux, overnight. Step II. Synthesis of NH₂-PEG-progesterone. Conditions: Progesterone, TFA (catalytic), MeOH, 40 °C, overnight. (B) ¹H NMR. (C) FTIR, (D) TLC ((A) NH₂-O-PEG-ONH₂, (B) co-spot, (C) NH₂-PEG-progesterone).

moieties arrange themselves in clusters.[52] The cluster effect enables the entire nanoparticle to acquire multiple homogeneous or heterogeneous functionalities that can detect different receptors simultaneously with enhanced targeting efficacy, as earlier reported.[50−52]

Herein, we report the development of a personalized hybrid imaging tool to visualize ITH in nonmetastatic breast cancer tumors. Our results show higher MTMPPPCAs uptake in the targeted tumor than in the untargeted. Furthermore, *in vivo* fluorescence biodistribution studies revealed the presence of estrogen receptor (ER+) and progesterone receptor (PR+) in the tumor site. *Ex vivo* PA imaging studies validated the fluorescence results. Furthermore, PA was able to differentiate the presence of both receptors in colocalized and non-colocalized areas. Immunohistochemistry (IHC) analysis confirmed the location of ER+ and PR+ visualized by fluorescence and PA imaging.

RESULTS AND DISCUSSION

Synthesis and Characterization of MTMPPPCAs. In this work, we have designed MTMPPPCAs endowed with high molecular specificity to detect LA and LB molecular subtypes. The MTMPPPCAs were synthesized following a self-assembly strategy shown in Figure 1. The PLGA shell surface was chemically modified with two unique targeting moieties, namely, NH₂-PEG-estrone and NH₂-PEG-progesterone, which bind specifically to the estrogen and progesterone receptors overexpressed in breast cancer cells. Near-infrared fluorophores such as indocyanine green (ICG) and squaraine 650 (SQ650) dyes formed the inner lining of the core and served as PA reporters.

The NH₂-PEG-estrone targeting moiety was synthesized by conjugating estrone ethyl glycolic acid (EGA) with the PEG-diamine molecule (Figure 2A). Derivatization of estrone was essential to construct an ideal position for conjugating the PEG-diamine molecule without hampering the binding affinity at the conjugation site of estrone. We modified the estrone molecule by synthesizing the estrone ester at the C-3 position with ethyl bromo ester under basic conditions. The further saponification reaction in the presence of sodium hydroxide resulted in the production of EGA in quantitative yields. The end group modification of PEG-diamine with EGA proceeded through regular amine-acid coupling chemistry using HATU as the coupling reagent. The conjugation of the modified estrone was demonstrated by the presence of aromatic proton signals at 6.81−7.19 ppm in the ¹H NMR spectrum (Figure 2B). FTIR analysis of NH₂-PEG-estrone revealed the presence of aromatic peaks of estrone around 1500 to 1600 cm⁻¹ (Figure 2C). The presence of carbonyl groups of estrone at the C-17 position along with the amide bond of modified estrone at C-3 with PEG-amine is observed from peaks present at the 1620 and 1742 cm⁻¹ bond. TLC showed the formation of the molecule (Figure 2D). The polar carboxylic acid functionalized EGA (R_f = 0.333) differed substantially upon conversion to the nonpolar NH₂-PEG-estrone (R_f = 0.777), confirming the successful conjugation of the estrone moiety with the PEG molecule.

The second targeting moiety, NH₂-PEG-progesterone, was initiated by a synthesis of the aminooxy PEG molecule (Figure 3A). Next, the ketone group of progesterone was conjugated with the aminooxy-PEG molecule *via* oxime formation. The oxime bond demonstrated higher stability compared to the other amine or hydrazine functionalities at physiological
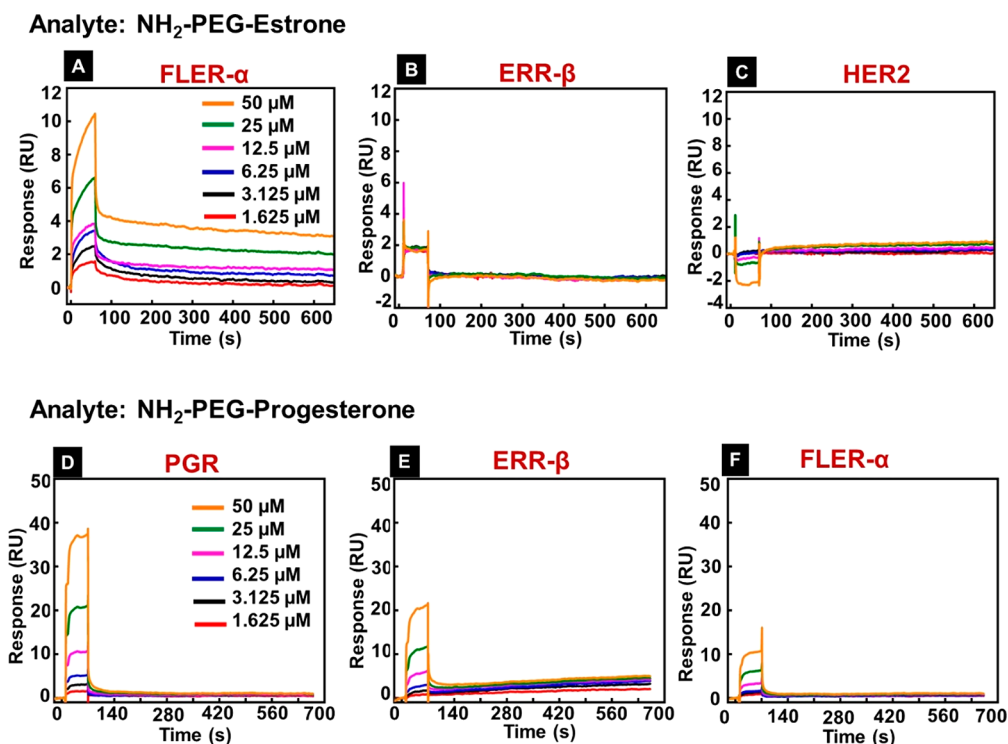
Figure 4. SPR sensorgrams. Top panel (A–C): (A) Binding affinity curves of NH$_2$-PEG-estrone with FLER-α. (B, C) ERR-β and HER2 are the negative controls for FLER-α. Bottom panel (D–F): (D) Binding affinity curves of NH$_2$-PEG-progesterone with progesterone receptor. (E, F) NH$_2$-PEG-progesterone cross-reacted a little with ERR-β and FLER-α.
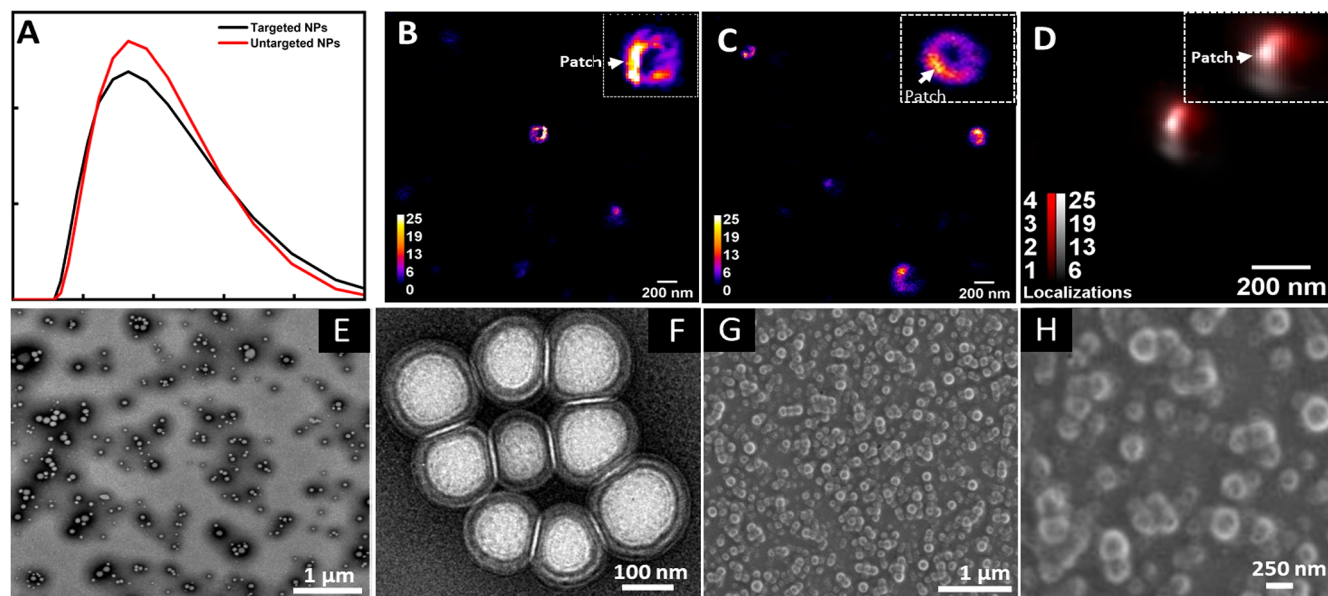
Figure 5. Physical characterization of MTMPPPPCAs. (A) Particle size distribution of MTMPPPPCAs and UTMPPPPCAs. 2D stochastic optical reconstruction microscopy (STORM) image of NP functionalized with NH$_2$-PEG-estrone-Alexa 647 (B), NH$_2$-PEG-progesterone-Cy3B (C), and NH$_2$-PEG-estrone-Alexa 647/NH$_2$-PEG-progesterone-Cy3B (D). The inset shows the patchy nature of MTMPPPPCAs and its hollow core. TEM (E, F) and SEM micrographs (G, H) exhibit the MTMPPPPCAs' morphology and surface structure, respectively.

conditions. The ^{1}H NMR peaks at 5.74 ppm (s, −CH), 4.15 ppm (m, −CH$_2$), and 3.64 ppm (bs, −CH$_2$) and the characteristic progesterone methyl peaks (−CH$_3$) at 2.12, 1.12, and 0.6 ppm were confirmed (Figure 3B). The FTIR peaks of NH$_2$-PEG-progesterone appeared at 1642 cm^{-1}, confirming the −C═N (imine) bond formation and validating the successful synthesis of NH$_2$-PEG-progesterone (Figure

3C). The TLC analysis demonstrated complete conjugation of progesterone with the aminooxy-PEG molecule (R_f = 0.422), as no traces of starting material were visible on the spot C of the reaction mixture compared to the starting material spot A (Figure 3D).

Receptor Specific Binding Affinity Studies Using Surface Plasmon Resonance (SPR). We used the SPR
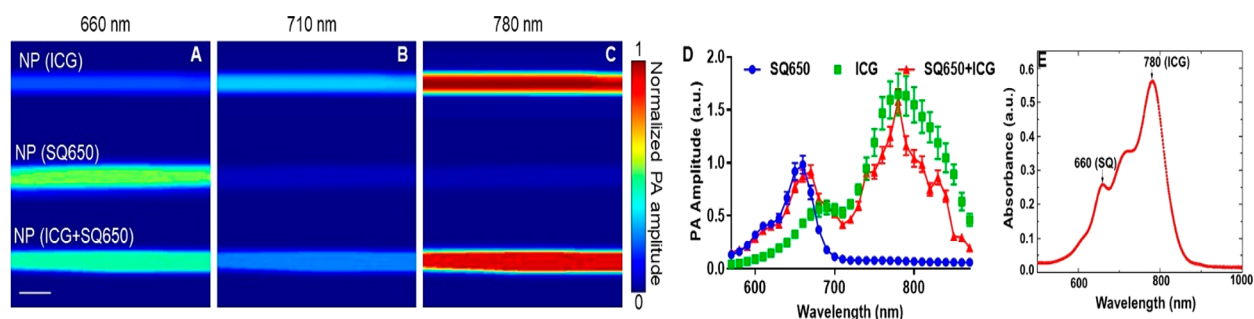
Figure 6. PA spectra of MTMPPPCAs. (A−C) PACT images of nanoparticles with ICG, nanoparticles with SQ650, and MTMPPPCAs in silicone tubes at wavelengths of 660, 710, and 780 nm, respectively. Scale bar, 1 mm. (D) PA spectra of MTMPPPCAs with ICG (green line), nanoparticles with SQ650 (blue line), and the MTMPPPCAs (red line). (E) Absorption spectrum of MTMPPPCAs.
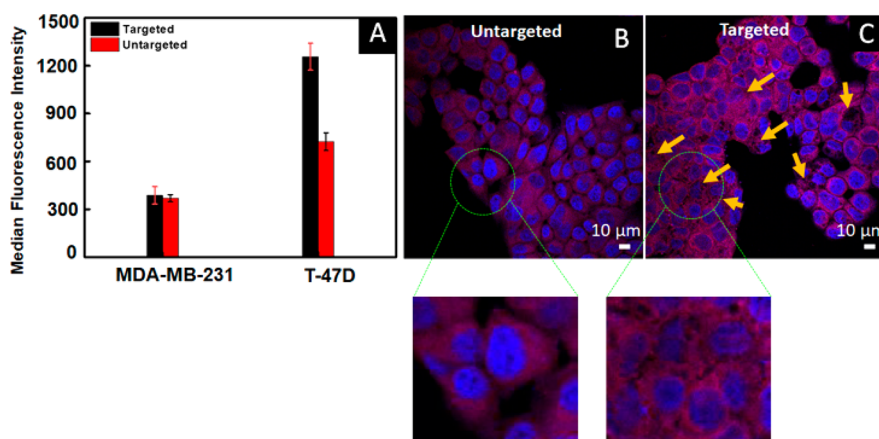
Figure 7. Cellular uptake studies of MTMPPPCAs and UTMPPPCAs in T-47D and MDA-MB-231 breast cancer cells. (A) The MTMPPPCAs uptake doubled after 24 h of incubation compared with UTMPPPCAs. Error bar, standard deviation (n = 3). (B, C) Confocal microscopy images of MTMPPPCAs cell uptake in T-47D cells after 24 h of incubation with the section insets. The yellow arrows point out the presence of MTMPPPCAs in the cytoplasm or nucleus of the cell. There is a higher cell uptake in the targeted sample compared to the untargeted one, as shown by the close-up images.

technique to assess the molecular specificity of NH$_2$-PEG-estrone and NH$_2$-PEG-progesterone (Figure 4). The SPR responses of the analyte (*i.e.*, NH$_2$-PEG-estrone) were plotted at different concentrations (Figure 4A−C). The SPR results show that the sharp shape of the sensorgrams in the association stage of the interaction indicates the binding of NH$_2$-PEG-estrone to full-length recombinant human estrogen alpha receptor (FLER-α) at different micromolar concentrations (Figure 4A). Fitting the sensorgram data to an appropriate kinetic binding model allowed the calculation of the kinetic disassociation (K_D) rate constant. Assuming 1:1 binding affinities and fitting the dose response plot revealed that the K_D value of FLER-α was 1.5 μM. This value indicates an excellent binding affinity between the analyte (*i.e.*, NH$_2$-PEG-estrone) and the ligand (*i.e.*, FLER-α). The fact that NH$_2$-PEG-estrone shows little binding or negligible binding to estrogen-related receptor beta (ERR-β) (Figure 4B) or HER2 (negative controls) (Figure 4C), respectively, demonstrates the preferential binding of NH$_2$-PEG-estrone to FLER-α. With respect to the molecular interaction between NH$_2$-PEG-progesterone and the PR, we observed specific binding at different concentrations, as shown in Figure 4 D−F. Following the same rationale described above, we found that the K_D for progesterone was 10 μM (Figure 4D−F). The binding affinity response was higher for NH$_2$-PEG-progesterone compared to ERR-β (Figure 4E) and FLER-α (Figure 4F) at different

concentrations, which suggests its molecular specificity with the progesterone receptor.

Physicochemical Characterization of MTMPPPCAs. A self-assembled construct with the targeting moieties on the PLGA shell surface and the PA reporter dyes forming the inner lining of the MTMPPPCAs' core was successfully achieved. The mean diameters of MTMPPPCAs and untargeted multiplexed patchy polymeric PA contrast agents (UTMPPP-CAs) were 169.3 ± 5.6 nm and 180.1 ± 2.4 nm respectively, showing a narrow size distribution (Figure 5A). The average zeta potentials of both targeted and untargeted nanoparticles were −21.4 ± 1.7 mV and −23.03 ± 1.33 mV, correspondingly (Figure S1). Furthermore, the mean particle size of MTMPPPCAs suspended in 1× PBS did not change within 21 days, exhibiting excellent long-term size stability (Figure S2). Two-dimensional stochastic optical reconstruction microscopy (STORM) images clearly showed the patchy nature of the MTMPPPCAs' surface (Figure 5B−D). The donut-like shape confirmed the MTMPPPCAs' hollow core structure (Figure 5B−D). The presence of NH$_2$-PEG-estrone-Alexa 647 and NH$_2$-PEG-progesterone-Cy3B is observed in both the nanoparticle's surface and patch, but it is more prominent in the latter, as shown in Figures 5B and C, respectively. The single-labeled experiments served as control samples for the two-color experiment. The dual STORM imaging experiment is presented in Figure 5D. In this picture, the presence of NH$_2$-PEG-estrone-Alexa-647/NH$_2$-PEG-progesterone is indicated

in white and red colors, respectively. These results suggest that the MTMPPPCA patch is formed by a heterogeneous mixture of both PEGylated targeted moieties. Additional characterization was performed by electron microscopy. TEM and SEM studies show the spherical-like shape and monodisperse characteristic of the synthesized MTMPPPCAs (Figure 5E–H). To assess the MTMPPPCAs' PA imaging performance, we conducted phantom studies and absorbance measurements.[53] Figure 6A shows the PA images of nanoparticles with ICG, nanoparticles with SQ650, and MTMPPPCAs. Both PA and optical absorption spectra exhibit two peaks at 660 and 780 nm, corresponding to the presence of SQ650 and 780 ICG, respectively (Figure 6D,E). The PA spectra of ICG and SQ650 were used for the spectral unmixing computation. The encapsulation efficiency (EE) for SQ650 and ICG was calculated as 55% and 46% (SI eq 2), respectively. The encapsulation results correlate well with the PLGA copolymer ratio (75:25) used during the nanoparticle synthesis.

***In Vitro* Assessment of the Cell Uptake of MTMPPPCAs in T-47D and MDA-MB-231 Breast Cancer Cell Lines.** The MTMPPPCAs' receptor-specific targeting capabilities were evaluated by incubating them with human breast cancer cell lines: (1) T-47D cells (ER+ and PR+) and (2) MDA-MBA-231 (ER−, PR−, HER2−). Cell uptake was assessed *via* the fluorescence-activated cell sorting (FACS) technique. The results in Figure 7A show significantly increased median fluorescence intensity (MFI) upon uptake by the T-47D cells (1250 au) compared to MDA-MB-231 cells (400 au) after 24 h of incubation. The receptor-mediated cell uptake of MTMPPPCAs is statistically significant ($p < 0.05$) in the T-47D compared to the MDA-MB-231 cells. Furthermore, the cell uptake results validated the specific binding of NH$_2$-PEG-estrone and NH$_2$-PEG-progesterone with ER+ and PR+ determined with SPR (Figure 4A–F). Notably, even though the internalization of UTMPPPCAs was observed in both cell lines, the MFI was lower than the targeted counterparts, which is attributed to the passive uptake of MTMPPPCAs in the tumor cells. The site-specific internalization of MTMPPPCAs was visualized and validated by confocal microscopy (Figure 7B,C). A higher accumulation of MTMPPPCAs was observed in the cytoplasm or nucleus of the breast cancer cells than that of the UTMPPPCAs. Overall, these results demonstrate the *in vitro* targeting ability of MTMPPPCAs to bind specifically to T-47D breast cancer tumor cells that overexpress ER+ and PR+.

Assessment of the Cellular Toxicity of MTMPPPCAs. A dose-dependent cell viability study was performed to assess the cellular toxicity of MTMPPPCAs. We evaluated the percent of T-47D cancer cell viability in the presence of the MTMPPPCAs at different concentrations and compared with that of UTMPPPCAs and targeted patchy polymeric nanoparticles (TPPNPs). TPPNPs is the control nanoparticle sample (*i.e.*, nanoparticles functionalized with the targeting moieties but not loaded with PA reporters). As shown in Figure 8, more than 90% of T-47D cells were still alive after being exposed to MTMPPPCAs at different concentrations for 24 h, suggesting that MTMPPPCAs are not toxic at the cellular level.

***In Vivo* Assessment of Targeting Efficacy of MTMPPPCAs in an Orthotopic Cell Line-Derived Xenograft (CDX) Breast Cancer Model.** We further investigated the targeting efficacy of MTMPPPCAs using an orthotopic CDX breast cancer model *in vivo* (Figure 9). We
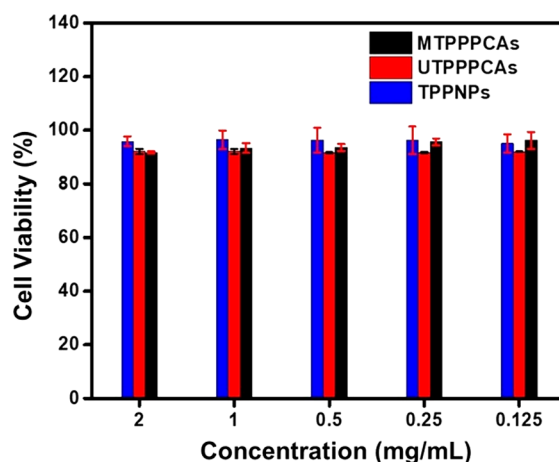
Figure 8. *In vitro* evaluation of the cellular toxicity of MTMPPPPCAs. Cell toxicity assessment of T-47D cells in the presence of MTMPPPCAs, UTMPPPCAs, and TPPPNPs (control) after 24 h of incubation at concentrations ranging from 0.125 to 2 mg/mL. Results are presented as percentage cell viability (mean ± SD) from three independent experiments.

implanted 7×10^6 freshly harvested human breast cancer cells (T-47D or MDA-MB-231) in the fourth abdominal mammary fat pad of six female athymic nude mice. When the tumor reached an average volume of 70 mm^3, we administered 1200 μg of a combination dose of MTMPPPCAs *via* tail-vein injection. The targeted nanoparticles (TNP) combination dose was composed of (TNP+SQ650+estrone, TNP+SQ650+ICG +progesterone+estrone, and TNP+SQ650+ICG+estrone) to differentiate ER+ from PR+ through the fluorescence and PA signals emitted by SQ650 and ICG. Real-time biodistribution studies were performed to assess the *in vivo* targeting efficacy of MTMPPPCAs functionalized with NH$_2$-PEG-estrone and NH$_2$-PEG-progesterone. The ER was localized and visualized by SQ650 (Figure 9 top panel), while the PR was visualized by ICG (Figure 9 bottom panel). Another group of six female mice was administered with UTMPPPCAs with a combination dose of untargeted nanoparticles (UTNP) (UTNP+ICG +SQ650, UTNP+ICG, UTNP+SQ650). In the third group, we injected a combination dose of MTMPPPCAs in MDA-MB-231 tumor-bearing mice (negative control group). The mice were imaged with the *in vivo* Imaging System (IVIS) at 1, 3, and 6 h post-injection. We detected the presence of SQ650 and ICG in the MTMPPPCAs and UTMPPPCAs.

When comparing the biodistribution profile of the T-47D tumor-bearing mice with MDA-MB-231 tumors based on the presence of SQ650 in the mice at the dorsal position, we observed that more nanoparticles were circulating in the bloodstream at all time points than that in the negative control group (Figure 9, top and bottom panels). The results were expected because the MTMPPPCAs were designed to bind specifically to cancer cells overexpressing ER and PR. MDA-MB-231 tumors do not express any of these receptors. Thus, it was expected to observe nanoparticle accumulation in the liver, spleen, kidneys, and intestines as corroborated in the ventral position of the untargeted mice in the negative control group (Figure 9, top and bottom panel, left and right sides). Also, we observed more nanoparticle uptake in the liver and spleen of the targeted mice in the negative control group than that of the targeted testing group, as shown in the biodistribution profile

SQ650
Ex= 675 nm, Em= 694 nm

Dorsal   **Ventral**

T-47D   MDA-MB-231   T-47D   MDA-MB-231

ICG
Ex=745 nm, Em=810 nm

Dorsal   **Ventral**

T-47D   MDA-MB-231   T-47D   MDA-MB-231
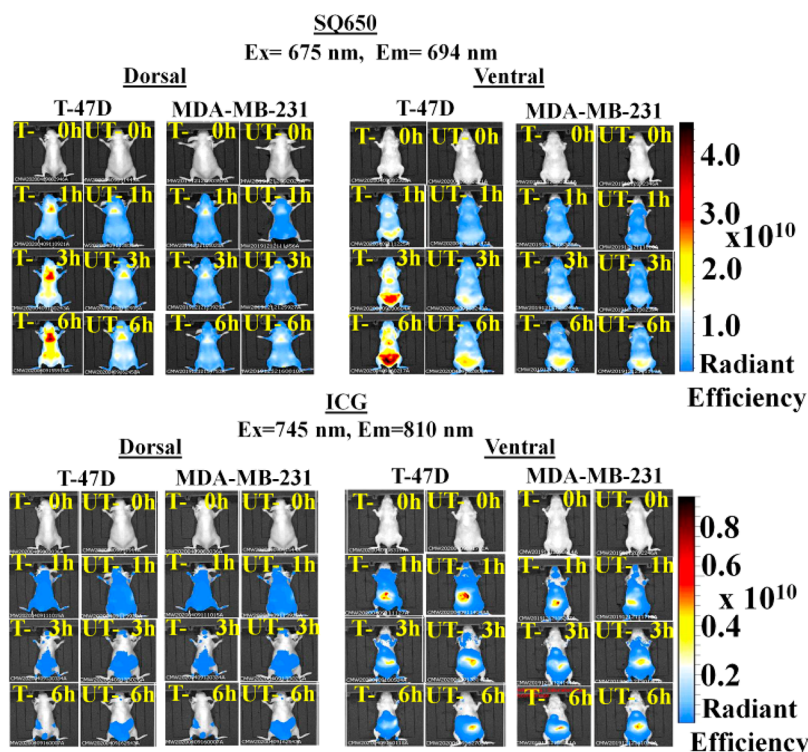
Figure 9. *In vivo* biodistribution studies. Mice were administered with a combination dose of MTMPPPCAs (T) and UTMPPPCAs (U) in T47-D tumors and MDA-MB-231 tumors (negative control) and imaged by the IVIS system at 1, 3, and 6 h time points. Biodistribution studies using 675 and 694 nm as the excitation and emission wavelengths, respectively, detected the presence of the SQ650. The images were taken at both dorsal and ventral positions. Biodistribution studies using 745 and 810 nm as the excitation and emission wavelengths, respectively, detected the presence of the ICG.

obtained with the ICG fluorescence signal (Figure 9, bottom panel, left and right sides).

Furthermore, in both the testing and negative control groups, medium fluorescence signals of free SQ650 were observed in the kidneys, urinary bladder, and intestines at 3 and 6 h time points (Figure 9, upper panel), suggesting that part of SQ650 leaks out from the polymeric matrix. Free ICG accumulated in the liver and spleen was also observed in both groups (Figure 9, bottom panel). Notably, despite the mice receiving a high dose of MTMPPPCAs, no signs of toxicity were observed in the animals. The *in vivo* biodistribution studies revealed that the ICG and SQ650 are cleared out from the mice's body primarily *via* the liver and urinary bladder, reinforcing the safety aspect of MTMPPPCAs. Thus, enhanced uptake was detected in MTMPPPCAs' tumor compared to that of UTMPPPCAs, highlighting the molecular specificity and the highly vascularized nature of the implanted breast tumors. The difference in the fluorescence signal emitted by SQ650 and ICG can be higher if the EE is increased by improving the polymer matrix's dye stability. Naked ICG and SQ650 leaked out from the PLGA nanoparticles during *in vivo* testing. Hence, further improvements can be made in the next generation of MTMPPPCAs.

Assessment of *Ex Vivo* Targeting Efficacy of MTMPPPCAs. The *in vivo* biodistribution studies show that MTMPPPCAs or UTMPPPCAs tend to accumulate in tumors and off-target organs (*i.e.*, liver, spleen, urinary bladder, and kidneys). These results were confirmed by the *ex vivo* biodistribution studies, which allowed us to investigate further the tumor uptake of MTMPPPCAs. The *ex vivo* analysis was performed immediately 6 h after injection. Fluorescence signals

from organs such as tumors, hearts, spleens, lungs, urinary bladders, and kidneys were obtained for both targeted and untargeted T-47D tumor-bearing mice. Significant uptake of MTMPPPCAs in the T-47D tumor was observed at 6 h postinjection for SQ650, while the fluorescence intensity of ICG was moderately low (Figure 10). The uptake of
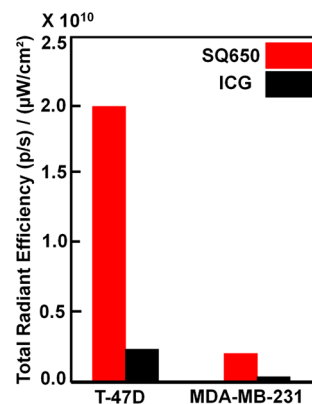
Figure 10. *Ex vivo tumor* uptake studies. MTMPPPCAs uptake by T-47D and MDA-MB-231 (negative control) tumors registered with SQ650 and ICG.

untargeted particles in the T-47D tumor was lower than that of the targeted particles, indicating the site-specific internalization of MTMPPPCAs. The lower uptake of untargeted particles in the tumor tissue occurs due to the enhanced permeability effect (EPR) of the tumor. Notably, the corresponding *ex vivo* image clearly showed a pronounced
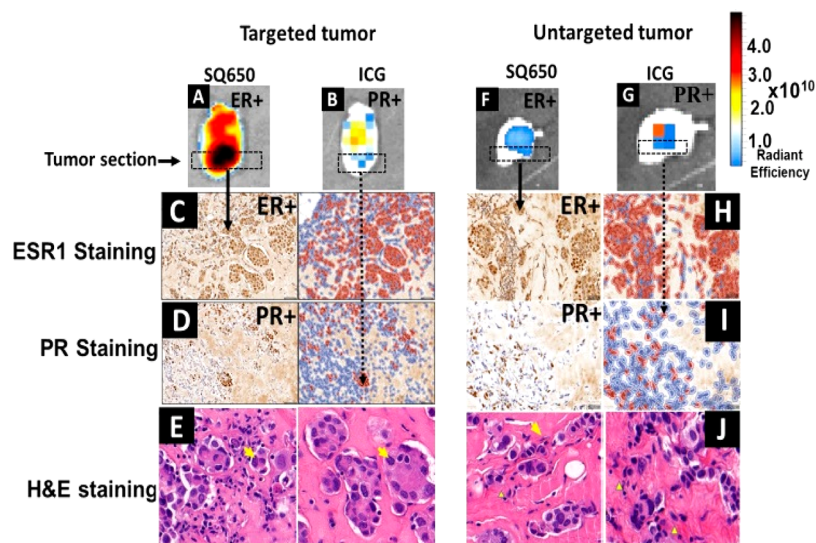
Figure 11. Visualization of ITH in *ex vivo* tumors using fluorescence imaging and validating these results with IHC. (A–G) Fluorescence images of targeted (A, B) and untargeted tumors (F, G) in which ER+ and PR+ were detected with SQ650 and ICG, respectively. More MTMPPPCA uptake in the targeted tumor was observed than that of the untargeted tumor. IHC studies confirm the presence of ER+ and PR+ in both targeted (C, D) and untargeted tumors (H, I) by staining the tumor breast cancer cell nuclei (brown areas). This figure portrays magnified pictures taken from the tumor sections indicated in (Figure 10A,B,F,G). The tumor sections were formalin-fixed paraffin embedded and immunostained separately with a primary anti-estrogen receptor 1 (ESR1) and anti-progesterone antibodies (PR). ER+ and PR+ were visualized with 3,3-diaminobensidine (DAB) (brown color). (E–J) Representative images of hematoxylin and eosin staining on FFPE showing the nuclei (blue) and cytoskeleton (pink) of the tumor breast cancer cells. The scale bar is 50 μm.
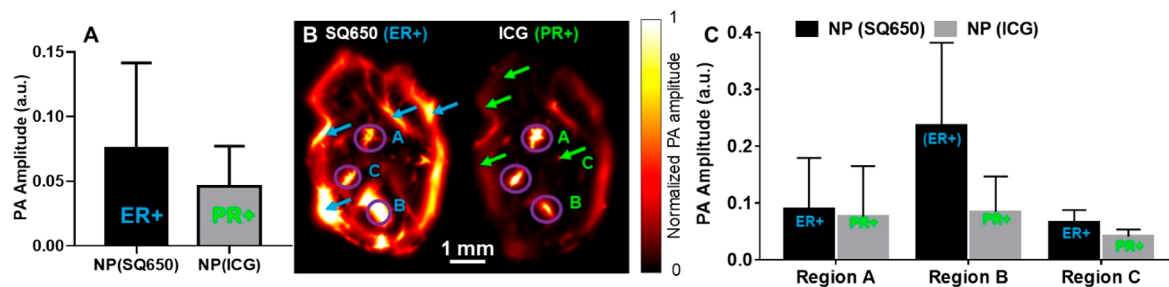
Figure 12. PA evaluation of MTMPPPCAs in the tumor *ex vivo*. (A) PA signals from SQ650 and ICG, computed by spectral unmixing. (B) PA images showing the distribution and localization of ER+ and PR+ receptors in the tumor *via* spectral unmixing. (C) Comparison of ER+ and PR+ in PA amplitude in colocalized regions.

tumor uptake of MTMPPPCAs in the T-47D tumor (Figure 10), confirming the molecular specificity property of the engineered contrast agents. Accumulation of NPs was observed in other organs, including liver, spleen, lungs, urinary bladder, and kidneys for both targeted and untargeted NPs, showing the regular uptake effect of the reticuloendothelial system (RES). Importantly, the administration of a combination dose comprised of a single or double targeting moiety as well as PA receptors helped to locate the ER and PR in the tumor region. Thus, the *ex vivo* tumor uptake results demonstrated that the engineered MTMPPPCAs could specifically accumulate in the tumor due to the ER+ and PR+ mediated receptor–ligand interaction, thereby yielding an enhanced imaging effect of contrast agents.

Visualization of ITH in Tumors *Ex Vivo*. The ER and PR receptor-specific internalization and distribution of MTMPPPCAs within the tumor sections were identified and visualized with fluorescence imaging and validated with IHC and hematoxylin and eosin (H&E) staining studies. The receptor-specific tissue penetration and distribution of targeted MTMPPPCAs (Figure 11A–D) were clearly observed

throughout the T-47D tissue section using the qualitative immunohistochemistry (IHC) analysis, and the untargeted counterparts are shown in Figure 11F–I. The localization of estrogen receptor one (ESR1) and progesterone receptor (PR) was evident, as shown by the brown stains in the targeted group, suggesting that MTMPPPCAs were distributed evenly between the intracellular and intercellular compartments of the tumor tissue. The results also revealed the exact localization of the ER and PR receptors in the tumoral region, which agreed with the fluorescent imaging results (Figure 10A,B,F,G). The colocalization of ER and PR in the tumor site was differentiated based on the staining pattern for ESR1 and PR antigens. For the untargeted nanoparticles, lower tracer activity was observed in the tumor. The H&E results (Figure 11E–J) confirmed the overall morphology of tumor cells, where eosinophilic color represents the cytoplasm and dark purple represents nuclei. The tumors exhibited significant stroma (dark pink areas) with the presence of extracellular fibrous matrix, and the cells were arranged in clusters (Figure 11E) and strands (Figure 11J). No cell toxicity induced by MTMPPPCAs was found with histology studies (Figures

S3−S5). A higher level of ER+ and PR+ was detected in the targeted tumor than that of the untargeted tumor, matching well with the fluorescence results.

***Ex Vivo* PA Imaging.** MTMPPPCAs loaded with two PA reporters (SQ650 and ICG) were used to identify the presence of ER+ and PR+ receptors inside the breast tumor. We embedded the excised tumor in agarose gel and imaged it at two peak wavelengths. The light was illuminated from the top onto the tumor for PA excitation. During PA imaging, the tumor was placed in the center of the full-ring ultrasonic transducer array. By elevational scanning the tumor across the focal plane of the transducer array, we obtained a series of cross-sectional images of the tumor. The PA images shown in Figure 12 are the integration projections of cross-sectional images of the tumor. Next, we performed spectral unmixing to accurately separate the photoacoustic signals of SQ650 and ICG, revealing the intratumor heterogeneity in Figure 12A−C. Figure 12A shows the averaged PA amplitude of SQ650 and ICG inside the tumor, illustrating the presence of ER+ and PR + receptors in the breast tumor. A spectral unmixed PA image of the tumor, as shown in Figure 12B, maps the distributions of ER+ and PR+. Figure 12B also revealed colocalization areas (purple circles), where both receptors are present in the same tumor site. By segmenting the colocalization areas (regions A, B, and C in Figure 12B), we found the PA signals from SQ650 in different parts of the tumor were higher than those of ICG, indicating that the tumor is predominantly ER+ (Figure 12C).

Biosafety Aspect of MTMPPPCAs. It is important to investigate the biosafety aspect of MTMPPPCAs to achieve their medical translation. The hemolytic assay shows that the highest (12 mg/mL) and lowest concentrations (1.3 mg/mL) of MTMPPPCAs induced 4.1% and 2.1% hemolysis, respectively (Figure 13). Thus, at these concentrations, MTMPPPCAs are slightly hemolytic and may not be compatible with blood. However, pathology studies of the targeted, untargeted, and control group (*i.e.*, no MTMPPPCAs administration) showed the absence of macrophages and necrotic tissue, which indicates no tissue toxicity (Figure 14).
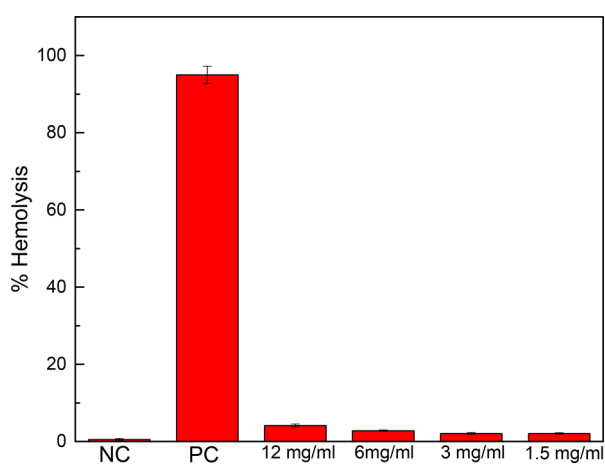
Figure 13. Hemolysis percent of MTMPPPCAs at different concentrations compared with the negative and positive controls. Diluted total blood hemoglobin in Ca^{2+}/Mg^{2+}-free PBS and Triton X-100 (10 mg/mL) are the negative and positive control, respectively. The highest (12 mg/mL) and lowest (1.3 mg/mL) concentrations induced 4.1% and 2.1% hemolysis, correspondingly. Thus, MTMPPPCAs at these concentrations are not compatible with blood.

Furthermore, the cell viability assay does not show levels of toxicity either. Overall, these results suggest that MTMPPPCAs are not toxic at the cellular and tissue levels but not blood compatible at those concentrations.

CONCLUSION

Our synthesized MTMPPPCAs showed excellent receptor-specific targeting efficiency in the ER+ and PR+ breast tumors with rapid internalization and accumulation and significant particle clearance profile. The *in vitro*, *in vivo* fluorescence, and *ex vivo* PA studies, in corroboration with the IHC analysis, demonstrated the feasibility of the MTMPPPCAs/SIP-PACT imaging technology to simultaneously visualize breast cancer biomarkers of different molecular subtypes with high molecular specificity. Furthermore, the toxicity assessment suggests that MTMPPPCAs are not toxic at the cellular and tissue levels, but may not be blood compatible at specific concentrations. The optimization of MTMPPPCAs will be required to achieve their usage in clinical settings. The outlook will include the synthesis of two additional targeting moieties: HER2 and trophoblast cell-surface antigen 2 (Trop-2) to detect HER2-enriched cells and TNBC. This addition will require more contrast agents. Near-infrared-II probes provide diverse candidates for the contrast agent selection.

The development of multitargeting and multiplexed contrast agents that simultaneously can detect LA, LB, HER2-enriched cells, and TNBC at the metastatic stage can make a difference in the oncology field. At this stage cancer patients need regular scans and frequent adjustment of treatments that cannot be carried out with existing techniques. The MTMPPPCAs/SIP-PACT technology has the potential to address this clinical gap, as well.

MATERIALS AND METHODS

Materials. Estrone, progesterone, poly(ethylene glycol) (PEG, 3400 Da), poly(vinyl alcohol) (9000−10 000 Da), and Amicon Ultra centrifugal filters with MWCO 10 000 were purchased from Sigma-Aldrich, USA. All reagents and solvents were of analytical/HPLC grade and used as received. ICG dye was purchased from AdooQ Bioscience, USA. Squaraine 650 (SQ650) dye was synthesized using the reported method.[54] PLGA (75:25) was purchased from Lactel Absorbable Polymers, USA. Dialysis membranes (MWCO 3500) used for purification of modified PEG ligands were purchased from Spectra Por-3, USA. Receptors required for SPR binding affinity analysis such as the recombinant protein of human progesterone receptor (PGR) was purchased from Origene, USA; full-length ER alpha recombinant protein receptor, Gibco human recombinant insulin, Gibco fetal bovine serum, trypsin-EDTA (0.25%) phenol red, enzyme-free sterile phosphate-buffered saline (PBS), and Invitrogen cell tracker red CMTPX dye were obtained from Thermo Fisher Scientific, USA. The T-47D cells, MDA-MB-231 cells, RPMI-1640 medium, Leibovitz's L-15 medium, and sterile DMSO were purchased from American Type Culture Collection (ATCC), USA. Zombie Violet fixable viability kit was obtained from Biolegend, USA. CytoTox-Fluor cytotoxicity assay kit was purchased from Promega, USA. High-concentration and LDEV-free matrigel for tumor implantation were purchased from Corning Life Sciences, USA.

The ^1H NMR experiments (δ scale) were carried out on a Jeol JNM-ECP Series Fourier transform NMR system at a magnetic field strength of 9.4 T, operating at 400 MHz. The ^1H NMR spectra were recorded in $CDCl_3$, D_2O, and DMSO-d_6, respectively. Fourier transform infrared (FTIR) spectroscopy characterization was performed using a Jasco FTIR 4100 spectrophotometer with a wavelength scanning range of 500−4000 cm^{-1}. The spectra were recorded using the optimum spectrometer parameters employing 36 scans per sample and a resolution of 4 cm^{-1}. SPR studies were
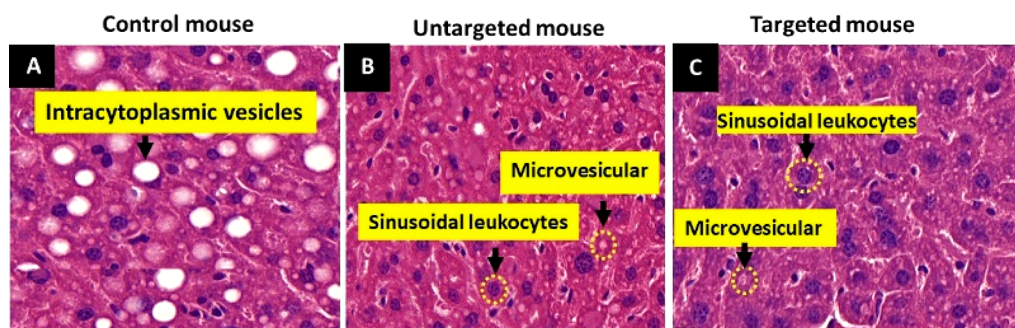
Figure 14. Hepatoxicity studies of MTMPPPCAs. H&E liver sections of control mouse (*i.e.*, no MTMPPPCAs administration) (A), untargeted mouse (B), and targeted mouse (C) were subject to pathology analysis. The pathology results show no evidence of liver toxicity caused by MTMPPPCAs because there is an absence of macrophages and necrosis. It should be noted that the control mouse (A) has a significant hepatocellular fatty change (minimal to mild, white circles) shown as intracytoplasmic vesicles. However, this phenomenon was not observed in the untargeted and targeted mice. Thus, the presence of hepacellular fatty change is not due to the MTMPPPCAs but to other factors. The presence of leuokocytes and microvesicles (in B and C) is due to the immunocompromised nature of the athymic nude mice.

performed using a Biacore T200 instrument with a CM5 chip at 25 °C. The nanoparticle size determination was performed using a Zetasizer Nano ZS from Malvern at 25 °C. The spectrum analysis was performed using an Agilent Cary 60 UV−vis spectrophotometer. Fluorescence measurements were carried out on a Shimadzu RF-6000 spectrofluorometer. TEM images were recorded using a FEI Talos TEM, operating at an 80 kV accelerating voltage. The SEM images of nanoparticles were recorded using a Zeiss Ultra 60 field emission scanning electron microscope. All animal experiments were carried out according to the guidelines of the Animal Ethics Committee of George Mason University (GMU). Athymic nude female mice (4−6 weeks old; 20−30 g body weight) were purchased from Jackson Laboratory and maintained at the Biomedical Research Laboratory, GMU (USA). Cultured fresh breast cancer cells were harvested and suspended in a solution of 50% matrigel and 50% 1× PBS for tumor implantation. About 7×10^6 cells/100 μL were injected subcutaneously near the fourth mammary gland in the abdominal cavity of the mice. The *in vivo* biodistribution studies were performed once the tumor volume reached ∼70 mm^3.

Synthesis of NH$_2$-PEG-Estrone. PEGylated estrone targeting moiety was synthesized *via* a stepwise route (Figure 2A). Initially, estrone was modified into its glycolic acid derivative for functionalization with PEG polymer (Figure 2A, step I). Estrone (100 mg, 0.37 mmol) was dissolved in 2 mL of tetrahydrofuran (THF), followed by sequential addition of potassium carbonate (306.8 mg, 2.22 mmol), 1.0 M tetrabutylammonium fluoride (TBAF) solution in THF (122 μL, 0.44 mmol), and ethyl bromoacetate (82 μL, 0.74 mmol). The reaction was heated at 40 °C. After 3 h, another portion of TBAF (122 μL, 0.44 mmol) and ethyl bromoacetate (82 μL, 0.74 mmol) was added and heating continued at 40 °C. The resultant product formation was monitored by TLC, ensuring complete conversion of the starting material (100% yield). After completion, THF was removed under reduced pressure, and the glycolate product was extracted using ethyl acetate (EtOAc) and H$_2$O. The crude glycolate product was then dissolved in 6 mL of a THF−H$_2$O (1:1) mixture. Sodium hydroxide (100 mg, 2.5 mmol) was added to the reaction mixture and stirred overnight at room temperature. The reaction mixture was concentrated by evaporating THF under reduced pressure. The resultant aqueous solution was acidified to pH 6.0 by adding 1.0 M HCl. Finally, the estrone glycolic acid product was extracted in EtOAc, and the aqueous phase was washed with EtOAc three times. The organic layers were combined and concentrated using a rotary evaporator to achieve the white solid product. ^{1}H NMR analysis of the obtained estrone glycolic acid derivative showed high purity with an overall yield of 90%, and it was used for further conjugation. ^{1}H NMR: δ 1.08 (3H, s), 1.38−1.79 (8H, m), 2.09−2.42 (4H, m), 2.60 (1H, ddd), 2.66−2.84 (2H, m), 4.45−4.46 (2H, s), 6.66 (1H, dd), 6.85 (1H, dd), 7.00 (1H, dd,).

The estrone glycolic acid derivative was conjugated with PEG diamine (NH$_2$-PEG-NH$_2$) using acid−amine coupling chemistry in the presence of HATU as the coupling reagent (Figure 2A, step II). Briefly, estrone glycolic acid (10 mg, 0.030 mmol) was added to a vial and was dissolved in 1 mL of anhydrous acetonitrile (ACN) followed by the addition of triethylamine (9.2 μL, 0.066 mmol). HATU (12 mg, 0.0315 mmol) was dissolved in 0.5 mL of dry acetonitrile and then added to the reaction vial. The reaction mixture was stirred for 15 min at room temperature under dark conditions. NH$_2$-PEG-NH$_2$ (102 mg, 0.030 mmol) was added followed by the addition of 2 mL of anhydrous ACN. The reaction was stirred overnight at room temperature. The reaction was monitored by TLC using 10% methanol (MeOH) + 1% ammonium hydroxide (NH$_4$OH). After completion, ACN was removed under reduced pressure, and the crude product was redissolved in 3 mL of d.H$_2$O. The solution was loaded into a dialysis bag (Spectra Por-3, MWCO 3500) and dialyzed against deionized water (2 × 2 L, 24 h). The solution was lyophilized, and 90 mg of NH$_2$-PEG-estrone conjugate was obtained. The obtained NH$_2$-PEG-estrone was analyzed using ^{1}H NMR, demonstrating the characteristic conjugated estrone peaks from δ 6.8 to 7.2 ppm.

Synthesis of NH$_2$-PEG-Progesterone. The synthesis proceeded by synthesizing an aminooxy derivative of PEG[55] due to the higher stability of the resultant oxime than that for the imine or hydrazone bonds at physiological conditions (Figure 3A, step I). First, an equimolar ratio of triphenylphosphine (0.308 g, 1.176 mmol) and N-hydroxyphthalimide (0.191 g, 1.176 mmol) were dissolved in THF (10 mL) and cooled to 0 °C under a N$_2$ atmosphere. PEG (3400 Da) (1.0 g, 0.294 mmol) was added to the cooled reaction mass. In a separate vial, a solution of diisopropyl azodicarboxylate (DIAD) (0.23 mL, 1.176 mmol) in THF (2 mL) was prepared and added dropwise to the above-mentioned reaction mixture at 0 °C. The reaction mixture was stirred overnight at room temperature. The reaction proceeded to completion in 12 h. The crude reaction mixture was thereafter concentrated under reduced pressure. The crude material was purified by flash chromatography by initially removing all the side products using a 70% EtOAc−hexane system, followed by using a 10% MeOH−DCM gradient to obtain the pure bis-N-hydroxyphthalimide-PEG derivative with 70% yield. ^{1}H NMR (400 MHz, CDCl$_3$): δ 7.83 (m, 4H, Ar), 7.44 (m, 4H, Ar), 4.36 (t, 4H, −CH$_2$), 3.85 (t, 4H, −CH$_2$), 3.63 (bs, 284H, −CH$_2$).

Next, the bis-N-hydroxyphthalimide PEG product (0.3 g, 0.081 mmol) was dissolved in DCM (10 mL). Hydrazine monohydrate (0.033 mL, 0.813 mmol) was added to the reaction mixture and refluxed overnight. The solvent was removed under reduced pressure. The crude mass was dissolved in a minimum amount of water, transferred to a dialysis bag (Spectra Por-3, MWCO 3500), and dialyzed against deionized water (2 × 2 L, 24 h). The aqueous layer was lyophilized to obtain the PEG-hydroxylamine derivative with 65%

yield. ^{1}H NMR (400 MHz, D_2O): δ 3.85 (t, 4H, $-CH_2$), 3.68 (bs, 284H, $-CH_2$).

The purified PEG-hydroxylamine (100 mg, 0.029 mmol) was dissolved in MeOH (6 mL) (Figure 3B, step II). Progesterone (36.67 mg, 0.116 mmol) and a catalytic amount of TFA (1−2 drops) were added to this solution. The reaction mass was heated at 40 °C overnight. After completion, MeOH was removed under reduced pressure, and the crude product was redissolved in 3 mL of d.H_2O. The solution was loaded into a dialysis bag (Spectra Por-3, MWCO 3500) and dialyzed against deionized water (2 × 2 L, 24 h). The solution was lyophilized to obtain the NH_2-PEG-progesterone conjugate with 90% yield. ^{1}H NMR (400 MHz, $CDCl_3$): δ 5.74 (s, 0.74H, −CH), 4.15 (m, 4H, $-CH_2$), 3.64 (bs, 315H, $-CH_2$), 3.0−0.5 (progesterone peak area with characteristic peaks $-CH_3$ at δ 2.12, 1.12, and 0.6).

Synthesis of MTMPPPCAs. Engineered MTMPPPCAs using the PEGylated targeting moieties (NH_2-PEG-estrone and NH_2-PEG-progesterone) were synthesized via a modified single-emulsification method described in Salvador-Morales et al.[50] Another batch of UTMPPPCAs (i.e., without the targeting moieties) was synthesized using the same procedure. Both targeted and untargeted NPs contained ICG and SQ650, which formed the inner lining of the core of the NP and also served as PA reporters. Starting materials were freshly prepared in appropriate solvents prior to NP synthesis. NP synthesis involves organic and aqueous phases. The organic phase is composed of PLGA (10 mg/mL in EtOAc), ICG (6.66 mg/mL in MeOH), and SQ650 (10 mg/mL in $CHCl_3$), while the aqueous phase is made of NH_2-PEG-estrone (1 mg/mL in d.H_2O), NH_2-PEG-progesterone (1 mg/mL in d.H_2O), NH_2-PEG-NH_2 (1 mg/mL in d.H_2O), and PVA (d.H_2O). MTMPPPCAs were synthesized via a stepwise fashion. Initially, an aqueous phase was prepared by mixing NH_2-PEG-estrone, NH_2-PEG-progesterone, PVA, and d.H_2O in a glass reaction beaker. Next, the organic phase was prepared separately, consisting of PLGA, ICG, SQ650, and MeOH. Finally, the organic phase was rapidly added to the aqueous phase, and the resultant suspension was mixed at 8000 rpm for 4 min using a homogenizer (L5M-A). The aqueous phase of UTMPPPCAs comprised NH_2-PEG-NH_2, PVA, and d.H_2O, while the organic phase was composed of PLGA, ICG, SQ650, and MeOH. UTMPPPCAs were synthesized following the same procedure described above. The excess of water and remnants of solvents were removed by evaporation and centrifugation. The latter was performed using Amicon Ultra centrifugal filters with an MWCO of 10 000 Da. The purified NP suspension was lyophilized to obtain the dried nanoparticles in quantitative yield, stored at −20 °C, and protected from light until further use.

Receptor-Specific Binding Affinity Studies Using SPR. The binding affinity of NH_2-PEG-estrone and NH_2-PEG-progesterone was assessed with a Biacore T200 system. FLER-α (66.4 kDa, ∼0.32 mg/mL stock) and recombinant PGR (98 kDa, ∼0.050 mg/mL stock) were used as ligands to take the SPR measurements. In the SPR experiment the FLER-α receptor and PGR receptor were covalently immobilized to flow cell 2 (FC2) of a CM5 sensor chip to ∼10 000 RU (response units) using standard amine coupling chemistry in the presence of 10 mM sodium acetate buffer at pH 5.5. ERR-β (54.3 kDa, ∼0.25 mg/mL stock) and full-length HER2 served as negative controls in the SPR experiment. Both ERR-β and HER2 were captured on flow cell 3 (FC3) and flow cell 4 (FC4) of the same sensor chip using standard amine coupling chemistry. PBS-P (20 mM PBS buffer pH 7.4, 137 mM NaCl, 2.7 mM KCl, 0.05% v/v surfactant P20) was used as the immobilization/capture running buffer. A similar procedure was followed to evaluate the binding affinity of NH_2-PEG-progesterone. ERR-β and FLER-α served as negative controls.

Flow cell 1 (FC1) was used as the reference for FC2, FC3, and FC4. The reference FC1 had the same coupling chemistry as the active FCs (FC2, FC3, and FC4) but without any proteins. NH_2-PEG-estrone and NH_2-PEG-progesterone analyte molecules with concentrations ranging from 1.625 to 50 μM were injected into these immobilized receptors overnight at a flow rate of 50 μL/min in the

presence of PBS-P buffer. After each injection, compounds were allowed to dissociate for 120 s before starting the next compound injection cycle. All targeting moieties were injected in triplicates. The contact and dissociation times used were 60 and 600 s, respectively. Binding affinities of NH_2-PEG-estrone and NH_2-PEG-progesterone were determined after subtracting the nonspecific binding to the reference surfaces and response values for the blank buffer injections (double reference subtraction). Theoretical maximum binding levels (R_{max}) were calculated assuming 1:1 binding interactions, and each molecule's binding percentage was compared to its corresponding R_{max} value. Molecules binding with more than 50% of the theoretical R_{max} values to FLER-α receptor and PGR receptor were selected as primary hits.

For the NH_2-PEG-estrone sample, dose-dependent response experiments were measured for FLER-α, ERR-β, and HER2 receptors immobilized on FC2, FC3, and FC4 using standard amine chemistry in the presence of 10 mM sodium acetate buffer at pH 5.5 to levels of ∼4900, ∼4900, and ∼1800 RU, respectively. Similarly, another dose−response experiment for NH_2-PEG-progesterone was recorded for PGR, ERR-β, and FLER-α receptors immobilized on FC2, FC3, and FC4 using standard amine chemistry in the presence of 10 mM sodium acetate buffer at pH 5.5 to levels of ∼9650, ∼4900, and ∼2600 RU, respectively. Sensorgrams from the overnight kinetics were evaluated, assuming 1:1 kinetic binding for determining the K_D values.

Physicochemical Characterization of MTMPPPCAs. *Super-resolution Imaging.* A 100 μg amount of Alexa Fluor 647 carboxylic acid and 100 μg of Cy3B NHS ester were covalently bound with NH_2-PEG-estrone and NH_2-PEG-progesterone, respectively, using the EDC/NHS coupling reagent as described in Invitrogen's protocol. Unreactive dyes were removed by dialysis for 24 h. Next, MTMPPPCAs were synthesized using the labeled PEGylated targeting moieties. The MTMPPPCAs were immobilized on 35 mm round glass coverslips using ultrasound gel, then mounted in Attofluor chambers. The chamber was filled with a PCA/PCD-based STORM buffer,[56] and the top sealed with a second coverslip, allowing oxygen to be depleted inside the chamber. Imaging was performed using a Nikon CFI Apochromat 100 ×/1.49 TIRF objective mounted on a Nikon Eclipse Ti-E inverted microscope. This microscope was equipped with a Perfect Focus System, 561 and 647 nm lasers at 500 mW each, and a Photometrics Evolve 512 EMCCD camera. Once the specimen was brought into focus and the TIRF angle was established, the Perfect Focus System was engaged, and the laser power was brought up to maximum. Once steady blinking of the fluorophores was established, 20 000−25 000 frames were acquired for each dye, and ThunderSTORM[57] was used for localization, drift correction, and visualization of the data.

Transmission Electron Microscopy (TEM). The MTMPPPCAs' morphology was determined by placing 10 μL of MTMPPPCA suspension on a copper−carbon grid followed by the addition of 10 μL of uranyl acetate (2% w/v) for negative staining purposes. The samples were dried at room temperature overnight and protected from light. After thorough drying, the samples were examined with an FEI Talos TEM, operated at an 80 kV accelerating voltage.

Scanning Electron Microscopy (SEM). The MTMPPPCAs' surface morphology was observed by SEM. Briefly, 10 μL of MTMPPPCA suspension was placed on a silicon wafer substrate, air-dried overnight, and coated with 60−40 Au−Pd. The samples were imaged with a Zeiss Ultra 60 FESEM operated at 1 kV.

Photoacoustic and Optical Absorption Spectra. We imbedded three tubes filled with nanoparticles with ICG, nanoparticles with SQ650, and MTMPPPCAs, respectively, in an agar gel phantom, which was imaged by PACT at wavelengths ranging from 570 to 870 nm. The wavelengths were generated by an OPO laser (Spitlight EVO III, Innolas, Inc.), which includes one pump laser and two OPO crystals. The fundamental wavelength of the pump laser is 1064 nm. Its second-harmonic wavelength (532 nm) pumped an NIR OPO to generate near-infrared light (680−1064 nm), while its third-harmonic wavelength (355 nm) pumped a VIS OPO to generate visible light (420−680 nm. Then the output wavelength can be switched between

660 and 780 nm by selecting the output from the corresponding OPO crystal. The PA signals of ICG and SQ650 were computed *via* spectral unmixing.

Absorption spectra of the nanoparticles with SQ650, nanoparticles with ICG, and an MTMPPPCA suspension were obtained on an Agilent Cary 60 UV−vis spectrophotometer. The absorption coefficient at λ_{max} = 650 nm (for SQ650) and λ_{max} = 780 nm (for ICG) were evaluated to determine the dye encapsulation for both NPs.

Particle Size and Zeta Potential. The dynamic light scattering (DLS) and zeta potential measurements were performed on a Malvern Zetasizer ZS (Nano-ZS90) instrument by dispersing the materials (1 mg/mL) in 1× PBS (0.15 M, pH 7.4) at 25 °C.

Determination of the Encapsulation Efficiency of the PA Reporters in the Polymeric Matrix. The encapsulation efficiency of the PA receptors in the polymeric particles was determined by fluorescence spectroscopy. Prior to the sample measurements, calibration curves for pure ICG and SQ650 dyes were recorded. ICG samples were prepared in d.H$_2$O with concentrations ranging from 100 to 1000 ng/mL. Fluorescence peaks for ICG were recorded at the excitation (λ_{exc}) wavelength of 780 nm and emission (λ_{em}) wavelength from 500 to 900 nm. Resultant λ_{em} values peaked at 806 nm were recorded. Based on the standard curve calculations, R^2 for ICG was 0.997, suggesting good linearity. In the case of SQ650 dye, the samples were prepared in MeOH owing to its hydrophobic character. SQ650 sample concentrations ranged from 50 to 400 ng/ mL and were recorded at the λ_{exc} = 650 nm and λ_{em} from 500 to 900 nm, respectively. The R^2 value for the SQ650 standard curve was 0.999. The subsequent dye encapsulation efficiency of the PA receptors in the polymeric matrix was calculated based on the standard curve equations for both ICG and SQ650. The resultant linear regression equation used to determine the encapsulation efficiency of ICG was $y = 0.0914X + 0.324$ (where y = fluorescence of sample at λ_{em} = 806 nm and X = concentration of sample), and that for SQ650 was $y = 343.350X + 2.884$ (where y = fluorescence of sample at λ_{em} = 662 nm and X = concentration of sample). Targeted and untargeted polymeric samples of known concentrations were suspended in 0.1 M sodium acetate buffer (pH 5.0) for 3 h before the measurements to achieve the complete degradation of NPs. These samples were further centrifuged to obtain the released dyes in the supernatant as well as the residue. Fluorescence measurements obtained for these samples were used to determine the overall encapsulation efficiency using the standard calibration curves as mentioned above and eq 2 (SI, 1.2).

In Vitro Cellular Uptake Studies. T-47D cells and MDA-MB-231 cells were cultured in their respective mediums as per ATCC standard protocols. Cells were grown at 37 °C in a humidified atmosphere with 5% CO$_2$. Cell uptake studies were performed using fluorescence-activating cell sorting (FACS) analysis and confocal microscopy. Binding affinity studies using FACS analysis were performed by seeding 3×10^5 cells per well in a 24-well culture plate. The cells were incubated for 24 h at 37 °C. The cells were washed with 1× PBS after 24 h. Thereafter, 500 μL of NP samples (0.5 mg/mL) in the complete medium was added to the cells and incubated for 24 h. The samples then were added in triplicates. After the incubation, the cells were washed with 1× PBS and collected in individual tubes after trypsinization and centrifugation. The cells were further incubated with Zombie Violet dye for 30 min at room temperature. After incubation, the cells were washed with 1× PBS and fixed with 4% paraformaldehyde buffer. After fixation, the cells were dispersed in fresh FACS buffer and analyzed using BD FACS Aria cell sorter as per the manufacturer's instructions. MFIs were recorded and plotted against the log-transformed NP concentrations using the nonlinear regression analysis in the Prism 7 software.

For the cellular uptake studies using confocal microscopy, 8×10^4 cells per well were seeded on glass coverslips placed in a 24-well culture plate and allowed to attach at 37 °C. After 24 h of incubation, cells were washed three times with 1× PBS and incubated with 500 μL of nanoparticle samples (0.5 mg/mL) in the complete medium for 24 h. After that, cells were washed three times with 1× PBS and

incubated for 30 min at 37 °C with 3 μM CMPTX cell tracker dye. After incubation, cells were washed with 1× PBS and fixed with 4% paraformaldehyde. Cells were washed several times with 1× PBS before and after staining with DAPI. Finally, the coverslips were mounted on microscope slides and examined by confocal laser scanning microscopy to determine the overall cellular uptake of MTMPPPCAs and UTMPPPCAs.

In Vitro Cytotoxicity Studies of MTMPPPCAs. The cell viability activity was measured using a CytoTox-Fluor cytotoxicity assay kit following the manufacturer's protocol. Briefly, T-47D and MDA-MB-231 cells were seeded in 96-well black microplates (1×10^4 cells per well) and incubated at 37 °C for 24 h for cell attachment. Wells were divided into a quintuplet group for each NP concentration of 2, 1, 0.5, 0.25, and 0.125 mg/mL. The entire set of experiments was performed in three independent studies to evaluate the experimental variability. Viability assay was evaluated for all concentrations at the 24 h time point following the manufacturer's guidelines. The percentile of cell viability was calculated using the resultant fluorescence values for each sample concentration. The standard equation for determining the cell viability percentile is provided in the SI, eq 1.

In Vivo MTMPPPCA Tumor Internalization Study Using an Orthotopic Cell-Derived Xenograft Breast Cancer Model. Athymic nude female mice bearing T-47D or MDA-MB-231 tumors were divided into two groups (six mice/group) based on the targeted or untargeted dose injected into the mice. The NP formulations were dissolved in sterile 1× PBS (pH 7.4) prior to the injections. The *in vivo* biodistribution profile was determined by administering a combination dose (1200 μg) of targeted nanoparticles (TNP) + SQ650 + estrone (400 μg), TNP + SQ650 + ICG + estrone (400 μg), and TNP + SQ650 + ICG + progesterone + estrone (400 μg). Similarly, a combination dose of UTMPPPCAs comprising untargeted NP (UNP) + SQ650 (400 μg), UNP + ICG (400 μg), and UNP + SQ650 + ICG (400 μg) was administered intravenously into the mice. A 100 μL amount of targeted or untargeted doses was injected into tumor-bearing mice *via* tail-vein injection. The mice were imaged by IVIS before (baseline) and postinjection at time points of 1, 3, and 6 h. The excitation and emission wavelengths of 675 and 694 nm were used for SQ650 and 745 and 810 nm for ICG. The mice were euthanized 6 h postinjection following the animal ethics committee regulations. *Ex vivo* fluorescence imaging of organs, including tumors, livers, spleens, kidneys, hearts, urinary bladders, and lungs, was analyzed using IVIS for determining the nanoparticle uptake.

Estrogen and Progesterone Receptor Immunofluorescence Staining. For pathology studies, T-47D mouse orthotopic xenograft *ex vivo* tumors with MTMPPPCAs and UTMPPPCAs were immediately stored in 10% formalin solution at room temperature after *ex vivo* fluorescence imaging. All the tumor tissue samples were analyzed for IHC using the ESR1 and PR antibodies. Breast cancer cells present in the tissue samples were identified using H&E stain. All tissue samples were processed and embedded with the largest surface area of the tumor down, mimicking the conditions for obtaining the fluorescent radiographs. All paraffin-embedded tumor tissue samples were sectioned at 4 μm thickness onto positively charged slides. After imaging the full tissue, 10 serial sections were collected for further staining to localize the estrogen and progesterone receptors.

IHC optimization for the ESR1 receptor was performed on the formalin-fixed paraffin-embedded (FPPE) human breast carcinoma tissue using a Leica Bond automated immunostainer and a rabbit anti-ESR1 antibody. Heat-induced antigen retrieval was performed using the Leica Bond epitope retrieval buffer (citrate solution, pH 6.0) for 20 min. Endogenous peroxides were blocked using the BloxAll (Vector Laboratories, SP-6000) for 20 min, followed by washing the tissue sections with buffer solution. Nonspecific antibody binding was blocked using the Novolink protein block (Leica, RE7280-CE) for 30 min, prior to the addition of the primary antibody. After 30 min of incubation with the primary antibody, the tumor sections were incubated with anti-rabbit poly-HRP-IgG secondary antibody (Leica, RE7280-CE) for 15 min. Anti-ESR1 antibody was detected using Novocastra Bond refine polymer detection and visualized with 3,3-diaminobenzidine stain as brown spots After the optimization process,

the slides were examined, and the optimal conditions to detect the antigen of interest were determined. It was found that a dilution of 1:100 and citrate pH 6.0 or antigen retrieval are the best conditions.

Similarly, the optimization of the PR receptor using IHC was performed on the FPPE human prostate tissue using a Leica Bond automated immunostainer and a rabbit anti-PR antibody. The optimization process for the detection of PR receptor in the tumor began at 1:100, 1:250, and 1:500. The rest of the procedure was the same as the one used for the detection of the estrogen receptor. It was found that the ideal dilution to detect PR was 1:100. PR+ cells appear as brown spots.

H&E Staining. The procedure was initiated by dewaxing the tumor tissue sections in xylene, followed by washing with 100% EtOH and then hydrating with 95% EtOH. The sections were rinsed twice with distilled water and incubated with the hematoxylin stain. After incubation, the sections were rinsed with running tap water and kept in the bluing solution for 10 s. These stained tissue sections were then rinsed with running tap water and placed in 95% EtOH for 1 min. Eosin staining was performed subsequently, followed by gradual dehydration of the stained tissues using 95% to 100% EtOH. Finally, the sections were cleared in xylene and mounted with Permaslip to obtain the images.

PA Measurements. Mapping the ITH in tumors *ex vivo* was conducted using the SIP-PACT system.[41] The SIP-PACT system employed a 512-element full-ring ultrasonic transducer array for 2D panoramic acoustic detection. A lab-made 512-channel preamplifier was directly connected to the ultrasonic transducer array housing to minimize cable noise. The preamplified PA signals were digitized using a 512-channel data acquisition system. The digitized radio frequency data were first stored in the onboard buffer, then transferred to a computer and reconstructed using the dual-speed-of-sound half-time universal back-projection algorithm.[29,41] The engineered MTMPPPCAs have two absorption peaks at 660 and 780 nm, respectively; thus the *ex vivo* PA measurements were carried out at 660 and 780 nm.

Hemolytic Assay. The hemolytic assay was performed as described by Neun B. *et al.*[58−60] This is a quantitative colorimetric assay to determine plasma-free hemoglobin and total hemoglobin in whole blood. In the first step, the levels of hemoglobin in a female human plasma sample were determined to ensure that no hemolysis occurred in the whole blood sample before the experiment. Thus, a calibration curve was prepared for this purpose. Briefly, 3 mL of female human fresh blood was centrifuged at 800g for 15 min. The supernatant was collected to determine the levels of hemoglobin in plasma, which was performed by preparing a calibration curve with calibration standards, quality controls, and control samples. Two hundred microliters of each calibration standard, quality control, and blank (cyanmethemo-globin (CMH)) were placed in a 96-well plate. Triplicates were used for each sample. A 200 μL amount of a total blood hemoglobin sample was prepared by mixing 20 μL of whole blood and 5.0 mL of CMH reagent, and 200 μL of this mixture was placed in each well. Samples were prepared in sextuples. A 100 μL amount of plasma-free hemoglobin were placed in a 96-well plate followed by 100 μL of CMH to make a final volume of 200 μL in each well. The absorbance was measured at 540 nm to determine the hemoglobin concentration in the plasma sample.

In the second step, the hemolysis percent caused by MTMPPPCAs was determined. The MTMPPPCAs were incubated with Total Blood Hemoglobin, diluted (TBHd) and without TBHd. Positive and negative controls were included in the experiment. The positive control samples were prepared by incubating TBHd samples with Triton X-100 (10 mg/mL), whereas the negative control samples consisted of incubating the TBHd samples in Ca^{2+}/Mg^{2+}-free PBS. The samples were placed in a water bath for 3 $1/4$ h followed by centrifugation at 800g for 15 min. The samples were mixed every 30 min. A fresh set of calibration and quality controls were prepared to determine the hemolysis caused by the presence of MTMPPPCAs in the samples incubated with TBHd. Subsequently, the absorbance was read at 540 nm to determine the samples' hemoglobin concentration.

Liver Pathology Studies. Three frozen mouse liver samples (livers from the untargeted, targeted, and control mouse (*i.e.*, no MTMPPPCA administration)) derived from the *ex vivo* animal studies were sectioned and stained with H&E according to Reveal Bioscience's protocol. The samples were subjected to pathology studies.

ASSOCIATED CONTENT

ⓢ Supporting Information

The Supporting Information is available free of charge at https://pubs.acs.org/doi/10.1021/acsnano.0c05893.

Additional experimental data including calculations for *in vitro* cytotoxicity assessment of MTMPPPCAs (eq 1), encapsulation efficiency of SQ650 and ICG (eq 2), zeta potential measurements (Figure S1), NP size stability studies (Figure S2), and pathology studies (Figures S3−S5) (PDF)

AUTHOR INFORMATION

Corresponding Author

Carolina Salvador-Morales − *Department of Chemistry & Biochemistry, George Mason University, Fairfax, Virginia 22030, United States;* ⓞ orcid.org/0000-0002-2588-6608; Email: csalvado@gmu.edu

Authors

Lei Li − *Caltech Optical Imaging Laboratory, Andrew and Peggy Cherng Department of Medical Engineering and Department of Electrical Engineering, California Institute of Technology, Pasadena, California 91125, United States*

Deepanjali Patil − *Department of Chemistry & Biochemistry, George Mason University, Fairfax, Virginia 22030, United States*

Greg Petruncio − *Department of Chemistry & Biochemistry, George Mason University, Fairfax, Virginia 22030, United States;* ⓞ orcid.org/0000-0002-2527-1064

Kathleen K. Harnden − *Inova Schar Cancer Institute, Fairfax, Virginia 22031, United States*

Jisha V. Somasekharan − *Research and Post Graduate Department of Chemistry, MES Keveeyam College, Valanchery, Kerala 676552, India*

Mikell Paige − *Department of Chemistry & Biochemistry, George Mason University, Fairfax, Virginia 22030, United States*

Lihong V. Wang − *Caltech Optical Imaging Laboratory, Andrew and Peggy Cherng Department of Medical Engineering and Department of Electrical Engineering, California Institute of Technology, Pasadena, California 91125, United States*

Complete contact information is available at:
https://pubs.acs.org/10.1021/acsnano.0c05893

Author Contributions

C.S.M. conceived the research idea and designed the research; C.S.M., L.L., and D.P. performed the research; C.S.M., L.L., and D.P. analyzed the data; C.S.M., L.L., D.P., and L.W. wrote the paper; G.P. and M.P. partially developed the organic synthesis of NH_2-PEG-estrone; J.S. synthesized the squaraine (SQ650) dye; K.H. provided clinical inputs.

Notes

The authors declare the following competing financial interest(s): In compliance with the George Mason University guidelines, C.S.M. discloses her financial interest in Nano-

REFERENCES

(1) Bray, F.; Ferlay, J.; Soerjomataram, I.; Siegel, R. L.; Torre, L. A.; Jemal, A. Global Cancer Statistics 2018: GLOBOCAN Estimates of Incidence and Mortality Worldwide for 36 Cancers in 185 Countries. *Ca-Cancer J. Clin.* 2018, 68, 394−424.

(2) Cronin, K. A.; Lake, A. J.; Scott, S.; Sherman, R. L.; Noone, A. M.; Howlader, N.; Henley, S. J.; Anderson, R. N.; Firth, A. U.; Ma, J. M.; Kohler, B. A.; Jemal, A. Annual Report to the Nation on the Status of Cancer, Part I: National Cancer Statistics. *Cancer* 2018, 124, 2785−2800.

(3) Joseph, C.; Papadaki, A.; Althobiti, M.; Alsaleem, M.; Aleskandarany, M. A.; Rakha, E. A. Breast Cancer Intratumour Heterogeneity: Current Status and Clinical Implications. *Histopathology* 2018, 73, 717−731.

(4) Tanas, A. S.; Sigin, V. O.; Kalinkin, A. I.; Litviakov, N. V.; Slonimskaya, E. M.; Ibragimova, M. K.; Ignatova, E. O.; Simonova, O. A.; Kuznetsova, E. B.; Kekeeva, T. V.; Larin, S. S.; Poddubskaya, E. V.; Trotsenko, I. D.; Rudenko, V. V.; Karandasheva, K. O.; Petrova, K. D.; Tsyganov, M. M.; Deryusheva, I. V.; Kazantseva, P. V.; Doroshenko, A. V.; et al. Genome-Wide Methylotyping Resolves Breast Cancer Epigenetic Heterogeneity and Suggests Novel Therapeutic Perspectives. *Epigenomics* 2019, 11, 605−617.

(5) Turashvili, G.; Brogi, E. Tumor Heterogeneity in Breast Cancer. *Front. Med.* 2017, 4, 1−11.

(6) American Cancer Society. Breast Cancer Facts & Figures 2019−2020. 2019, https://www.cancer.org/content/dam/cancer-org/research/cancer-facts-and-statistics/breast-cancer-facts-and-figures/breast-cancer-facts-and-figures-2019-2020 (accessed March 11, 2020).

(7) Sinn, H. P.; Kreipe, H. A Brief Overview of the WHO Classification of Breast Tumors, 4th Edition, Focusing on Issues and Updates from the 3rd Edition. *Breast Care* 2013, 8, 149−154.

(8) Fragomeni, S. M.; Sciallis, A.; Jeruss, J. S. Molecular Subtypes and Local-Regional Control of Breast Cancer. *Surg. Oncol. Clin. N. Am.* 2018, 27, 95−120.

(9) Dai, X.; Xiang, L.; Li, T.; Bai, Z. Cancer Hallmarks, Biomarkers and Breast Cancer Molecular Subtypes. *J. Cancer* 2016, 7, 1281−94.

(10) Gao, J. J.; Swain, S. M. Luminal A Breast Cancer and Molecular Assays: A Review. *Oncologist* 2018, 23, 556−565.

(11) Bertucci, F.; Finetti, P.; Goncalves, A.; Birnbaum, D. The Therapeutic Response of ER+/HER2- Breast Cancers Differs According to the Molecular Basal or Luminal Subtype. *NPJ. Breast Cancer* 2020, 6, 1−8.

(12) Schettini, F.; Pascual, T.; Conte, B.; Chic, N.; Braso-Maristany, F.; Galvan, P.; Martinez, O.; Adamo, B.; Vidal, M.; Munoz, M.; Fernandez-Martinez, A.; Rognoni, C.; Griguolo, G.; Guarneri, V.; Conte, P. F.; Locci, M.; Brase, J. C.; Gonzalez-Farre, B.; Villagrasa, P.; De Placido, S.; et al. HER2-Enriched Subtype and Pathological Complete Response in HER2-Positive Breast Cancer: A Systematic Review and Meta-Analysis. *Cancer Treat. Rev.* 2020, 84, 101965.

(13) Krasniqi, E.; Barchiesi, G.; Pizzuti, L.; Mazzotta, M.; Venuti, A.; Maugeri-Sacca, M.; Sanguineti, G.; Massimiani, G.; Sergi, D.; Carpano, S.; Marchetti, P.; Tomao, S.; Gamucci, T.; De Maria, R.; Tomao, F.; Natoli, C.; Tinari, N.; Ciliberto, G.; Barba, M.; Vici, P. Immunotherapy in HER2-Positive Breast Cancer: State of the Art and Future Perspectives. *J. Hematol. Oncol.* 2019, 12, 1−26.

(14) Zhao, S.; Zuo, W. J.; Shao, Z. M.; Jiang, Y. Z. Molecular Subtypes and Precision Treatment of Triple-Negative Breast Cancer. *Ann. Transl. Med.* 2020, 8, 1−14.

(15) Lee, J.; Yost, S.; Yuan, Y. Neoadjuvant Treatment for Triple Negative Breast Cancer: Recent Progresses and Challenges. *Cancers* 2020, 12, 1−20.

(16) Schmitz, J.; Schwab, J.; Schwenck, J.; Chen, Q.; Quintanilla-Martinez, L.; Hahn, M.; Wietek, B.; Schwenzer, N.; Staebler, A.; Kohlhofer, U.; Aina, O. H.; Hubbard, N. E.; Reischl, G.; Borowsky, A. D.; Brucker, S.; Nikolaou, K.; la Fougere, C.; Cardiff, R. D.; Pichler, B. J.; Schmid, A. M. Decoding Intratumoral Heterogeneity of Breast Cancer by Multiparametric *in Vivo* Imaging: A Translational Study. *Cancer Res.* 2016, 76, 5512−5522.

(17) Bailly, C.; Bodet-Milin, C.; Bourgeois, M.; Gouard, S.; Ansquer, C.; Barbaud, M.; Sebille, J. C.; Cherel, M.; Kraeber-Bodere, F.; Cartier, T. Exploring Tumor Heterogeneity Using PET Imaging: The Big Picture. *Cancers* 2019, 11, 1−17.

(18) Molina-Garcia, D.; Garcia-Vicente, A. M.; Perez-Beteta, J.; Amo-Salas, M.; Martinez-Gonzalez, A.; Tello-Galan, M. J.; Soriano-Castrejon, A.; Perez-Garcia, V. M. Intratumoral Heterogeneity in ^{18}F-FDG PET/CT by Textural Analysis in Breast Cancer as a Predictive and Prognostic Subrogate. *Ann. Nucl. Med.* 2018, 32, 379−388.

(19) Yoon, H. J.; Kim, Y.; Chung, J.; Kim, B. S. Predicting Neo-Adjuvant Chemotherapy Response and Progression-Free Survival of Locally Advanced Breast Cancer Using Textural Features of Intratumoral Heterogeneity on F-18 FDG PET/CT and Diffusion-Weighted MR Imaging. *Breast J.* 2019, 25, 373−380.

(20) Schelhaas, S.; Heinzmann, K.; Bollineni, V. R.; Kramer, G. M.; Liu, Y.; Waterton, J. C.; Aboagye, E. O.; Shields, A. F.; Soloviev, D.; Jacobs, A. H. Preclinical Applications of 3′-Deoxy-3′- [^{18}F] Fluoro-Thymidine in Oncology- A Systematic Review. *Theranostics* 2017, 7, 40−50.

(21) Liao, G. J.; Clark, A. S.; Schubert, E. K.; Mankoff, D. A. F-18-Fluoroestradiol PET: Current Status and Potential Future Clinical Applications. *J. Nucl. Med.* 2016, 57, 1269−1275.

(22) Groheux, D.; Martineau, A.; Teixeira, L.; Espie, M.; de Cremoux, P.; Bertheau, P.; Merlet, P.; Lemarignier, C. ^{18}FDG-PET/CT for Predicting the Outcome in ER+/HER2-Breast Cancer Patients: Comparison of Clinicopathological Parameters and PET Image-Derived Indices Including Tumor Texture Analysis. *Breast Cancer Res.* 2017, 19 (3), 1−10.

(23) Yildirim, N.; Simsek, M.; Aldemir, M. N.; Bilici, M.; Tekin, S. B. Relationship Between 18-FDG-PET/CT and Clinicopathological Features and Pathological Responses in Patients with Locally Advanced Breast Cancers. *Eurasian J. Med.* 2019, 51, 154−159.

(24) Groheux, D.; Cochet, A.; Humbert, O.; Alberini, J. L.; Hindie, E.; Mankoff, D. ^{18}F-FDG PET/CT for Staging and Restaging of Breast Cancer. *J. Nucl. Med.* 2016, 57, 17S−26S.

(25) Adejolu, M.; Huo, L.; Rohren, E.; Santiago, L.; Yang, W. T. False-Positive Lesions Mimicking Breast Cancer on FDG PET and PET/CT. *AJR, Am. J. Roentgenol.* 2012, 198, W304−W314.

(26) Yamamoto, S.; Yamagishi, S.; Kohno, T.; Tajiri, R.; Gondo, T.; Fujii, Y.; Tsukamoto, H. Maximum Standardized Uptake Value of ^{18}F-Fluorodeoxyglucose Positron Emission Tomography/Computed Tomography Could Replace Pathological Diagnosis in Luminal Breast Cancer. *Ann. Breast Surg.* 2019, 3 (5), 1410−1418.

(27) Li, L.; Shemetov, A. A.; Baloban, M.; Hu, P.; Zhu, L. R.; Shcherbakova, D. M.; Zhang, R. Y.; Shi, J. H.; Yao, J. J.; Wang, L. H. V.; Verkhusha, V. V. Small Near-Infrared Photochromic Protein for Photoacoustic Multi-Contrast Imaging and Detection of Protein Interactions *in Vivo*. *Nat. Commun.* 2018, 9 (2734), 1−14.

(28) Hai, P. F.; Imai, T.; Xu, S.; Zhang, R. Y.; Aft, R. L.; Zou, J.; Wang, L. H. V. High-Throughput, Label-Free, Single-Cell Photoacoustic Microscopy of Intratumoral Metabolic Heterogeneity. *Nat. Biomed. Eng.* **2019**, *3*, 381−391.

(29) Wu, Z. G.; Li, L.; Yang, Y. R.; Hu, P.; Li, Y.; Yang, S. Y. O.; Wang, L. V.; Gao, W. A Microrobotic System Guided by Photoacoustic Computed Tomography for Targeted Navigation in Intestines *in Vivo. Sci. Robot.* **2019**, *4* (eaax0613), 1−20.

(30) Yao, J. J.; Kaberniuk, A. A.; Li, L.; Shcherbakova, D. M.; Zhang, R. Y.; Wang, L. D.; Li, G.; Verkhusha, V. V.; Wang, L. H. V. Multiscale Photoacoustic Tomography Using Reversibly Switchable Bacterial Phytochrome as a Near-Infrared Photochromic Probe. *Nat. Methods* **2016**, *13*, 67−73.

(31) Weber, J.; Beard, P. C.; Bohndiek, S. E. Contrast Agents for Molecular Photoacoustic Imaging. *Nat. Methods* **2016**, *13*, 639−650.

(32) Bao, X.; Yuan, Y.; Chen, J.; Zhang, B.; Li, D.; Zhou, D.; Jing, P.; Xu, G.; Wang, Y.; Holá, K.; Shen, D.; Wu, C.; Song, L.; Liu, C.; Zbořil, R.; Qu, S. *In Vivo* Theranostics with Near-Infrared-Emitting Carbon Dots—Highly Efficient Photothermal Therapy Based on Passive Targeting After Intravenous Administration. *Light: Sci. Appl.* **2018**, *7* (91), 1−11.

(33) Li, L.; Zhu, L. R.; Shen, Y. C.; Wang, L. V. H. Multiview Hilbert Transformation in Full-Ring Transducer Array-Based Photoacoustic Computed Tomography. *J. Biomed. Opt.* **2017**, *22*, 076017-1−076017-7.

(34) Steinberg, I.; Huland, D. M.; Vermesh, O.; Frostig, H. E.; Tummers, W. S.; Gambhir, S. S. Photoacoustic Clinical Imaging. *Photoacoustics* **2019**, *14*, 77−98.

(35) Wang, L. H. V.; Yao, J. J. A Practical Guide to Photoacoustic Tomography in The Life Sciences. *Nat. Methods* **2016**, *13*, 627−638.

(36) Li, Y.; Li, L.; Zhu, L. R.; Maslov, K.; Shi, J. H.; Hu, P.; Bo, E.; Yao, J. J.; Liang, J. Y.; Wang, L. D.; Wang, L. H. V. Snapshot Photoacoustic Topography Through an Ergodic Relay for High-Throughput Imaging of Optical Absorption. *Nat. Photonics* **2020**, *14*, 164−170.

(37) Razansky, D.; Distel, M.; Vinegoni, C.; Ma, R.; Perrimon, N.; Koster, R. W.; Ntziachristos, V. Multispectral Opto-Acoustic Tomography of Deep-Seated Fluorescent Proteins *in Vivo. Nat. Photonics* **2009**, *3*, 412−417.

(38) Li, L.; Xia, J.; Li, G.; Garcia-Uribe, A.; Sheng, Q. W.; Anastasio, M. A.; Wang, L. V. Label-Free Photoacoustic Tomography of Whole Mouse Brain Structures *ex Vivo. Neurophotonics* **2016**, *3*, 035001-1−035001-8.

(39) Shi, J. H.; Wong, T. T. W.; He, Y.; Li, L.; Zhang, R. Y.; Yung, C. S.; Hwang, J.; Maslov, K.; Wang, L. H. V. High-Resolution, High-Contrast Mid-Infrared Imaging of Fresh Biological Samples with Ultraviolet-Localized Photoacoustic Microscopy. *Nat. Photonics* **2019**, *13*, 609−615.

(40) Beard, P. Biomedical Photoacoustic Imaging. *Interface Focus* **2011**, *1*, 602−631.

(41) Li, L.; Zhu, L. R.; Ma, C.; Lin, L.; Yao, J. J.; Wang, L. D.; Maslov, K.; Zhang, R. Y.; Chen, W. Y.; Shi, J. H.; Wang, L. H. V. Single-Impulse Panoramic Photoacoustic Computed Tomography of Small-Animal Whole-Body Dynamics at High Spatiotemporal Resolution. *Nat. Biomed. Eng.* **2017**, *1* (0071), 1−26.

(42) Lin, L.; Hu, P.; Shi, J. H.; Appleton, C. M.; Maslov, K.; Li, L.; Zhang, R. Y.; Wang, L. H. V. Single-Breath-Hold Photoacoustic Computed Tomography of the Breast. *Nat. Commun.* **2018**, *9*, 1−9.

(43) Toi, M.; Asao, Y.; Matsumoto, Y.; Sekiguchi, H.; Yoshikawa, A.; Takada, M.; Kataoka, M.; Endo, T.; Kawaguchi-Sakita, N.; Kawashima, M.; Fakhrejahani, E.; Kanao, S.; Yamaga, I.; Nakayama, Y.; Tokiwa, M.; Torii, M.; Yagi, T.; Sakurai, T.; Togashi, K.; Shiina, T. Visualization of Tumor-Related Blood Vessels in Human Breast by Photoacoustic Imaging System with a Hemispherical Detector Array. *Sci. Rep.* **2017**, *7*, 1−11.

(44) Diot, G.; Metz, S.; Noske, A.; Liapis, E.; Schroeder, B.; Ovsepian, S. V.; Meier, R.; Rummeny, E.; Ntziachristos, V. Multispectral Optoacoustic Tomography (MSOT) of Human Breast Cancer. *Clin. Cancer Res.* **2017**, *23*, 6912−6922.

(45) Dogan, B. E.; Menezes, G. L. G.; Butler, R. S.; Neuschler, E. I.; Aitchison, R.; Lavin, P. T.; Tucker, E. L.; Grobmyer, S. R.; Otto, P. M.; Stavros, A. T. Optoacoustic Imaging and Gray-Scale US Features of Breast Cancers: Correlation with Molecular Subtypes. *Radiology* **2019**, *292*, 564−572.

(46) Menezes, G. L. G.; Mann, R. M.; Meeuwis, C.; Bisschops, B.; Veltman, J.; Lavin, P. T.; van de Vijver, M. J.; Pijnappel, R. M. Optoacoustic Imaging of the Breast: Correlation with Histopathology and Histopathologic Biomarkers. *Eur. Radiol.* **2019**, *29*, 6728−6740.

(47) Wilson, K. E.; Bachawal, S. V.; Willmann, J. K. Intraoperative Resection Guidance with Photoacoustic and Fluorescence Molecular Imaging Using an Anti-B7-H3 Antibody-Indocyanine Green Dual Contrast Agent. *Clin. Cancer Res.* **2018**, *24*, 3572−3582.

(48) Deng, L. M.; Cai, X. J.; Sheng, D. L.; Yang, Y.; Strohm, E. M.; Wang, Z. G.; Ran, H. T.; Wang, D.; Zheng, Y. Y.; Li, P.; Shang, T. T.; Ling, Y.; Wang, F. J.; Sun, Y. A Laser-Activated Biocompatible Theranostic Nanoagent for Targeted Multimodal Imaging and Photothermal Therapy. *Theranostics* **2017**, *7*, 4410−4423.

(49) Feng, J.; Xu, Z.; Luo, D.; Liu, X. Multiplexed Imaging with Coordination Nanoparticles for Cancer Diagnosis and Therapy. *ACS Appl. Bio Mater.* **2020**, *3*, 713−720.

(50) Salvador-Morales, C.; Brahmbhatt, B.; Marquez-Miranda, V.; Araya-Duran, I.; Canan, J.; Gonzalez-Nilo, F.; Vilos, C.; Cebral, J.; Mut, F.; Lohner, R.; Leong, B.; Sundaresan, G.; Zweit, J. Mechanistic Studies on the Self-Assembly of PLGA Patchy Particles and Their Potential Applications in Biomedical Imaging. *Langmuir* **2016**, *32*, 7929−7942.

(51) Rasheed, N.; Khorasani, A. A.; Cebral, J.; Mut, F.; Lohner, R.; Salvador-Morales, C. Mechanisms Involved in the Formation of Biocompatible Lipid Polymeric Hollow Patchy Particles. *Langmuir* **2015**, *31*, 6639−6648.

(52) Salvador-Morales, C.; Valencia, P. M.; Gao, W.; Karnik, R.; Farokhzad, O. C. Spontaneous Formation of Heterogeneous Patches on Polymer-Lipid Core-Shell Particle Surfaces During Self-Assembly. *Small* **2013**, *9*, 511−517.

(53) Werner, J. P. F.; Huang, Y.; Mishra, K.; Chmyrov, A.; Ntziachristos, V.; Stiel, A. C. Challenging a Preconception: Optoacoustic Spectrum Differs from the Absorption Spectrum of Proteins and Dyes for Molecular Imaging. *BioRxiv* **2020**, 1−27.

(54) Khopkar, S.; Deshpande, S.; Shankarling, G. Greener Protocol for the Synthesis of NIR Fluorescent Indolenine-Based Symmetrical Squaraine Colorants. *ACS Sustainable Chem. Eng.* **2018**, *6*, 10798−10805.

(55) Collins, J.; Xiao, Z. Y.; Connal, L. A. Tunable Degradation of Polyethylene Glycol-Like Polymers Based on Imine and Oxime Bonds. *J. Polym. Sci., Part A: Polym. Chem.* **2017**, *55*, 3826−3831.

(56) Olivier, N.; Keller, D.; Gönczy, P.; Manley, S. Resolution Doubling in 3D-STORM Imaging Through Improved Buffers. *PLoS One* **2013**, *8* (e69004), 1−9.

(57) Ovesný, M.; Křížek, P.; Borkovec, J.; Švindrych, Z.; Hagen, G. M. ThunderSTORM: A Comprehensive ImageJ Plugin for PALM and STORM Data Analysis and Super-Resolution Imaging. *Bioinformatics* **2014**, *30*, 2389−2390.

(58) Neu, B. W.; Cedrone, E.; Dobrovolskaia, M. A. *NCL Method ITA-1: Analysis of Hemolytic Properties of Nanoparticles*; National Characterization Lab: Frederick, MD, 2020; pp 1−17.

(59) ASTM Standard Practice F 756-00. Assessment of Hemolytic Properties of Materials.

(60) ASTM E2524-08 (2013) Standard Test Method for Analysis of Hemolytic Properties of Nanoparticles.